The unconventional cytoplasmic sensing mechanism for ethanol chemotaxis in *Bacillus subtilis*

Payman Tohidifar[a], Girija A. Bodhankar[a], Sichong Pei[a], C. Keith Cassidy[c], Hanna E. Walukiewicz[ab], George W. Ordal[b], Phillip J. Stansfeld[d], Christopher V. Rao[a#]

[a]Department of Chemical and Biomolecular Engineering, University of Illinois at Urbana-Champaign, Urbana, Illinois, 61801, USA

[b]Department of Biochemistry, University of Illinois at Urbana-Champaign, Urbana, Illinois, 61801, USA

[c]Department of Biochemistry, University of Oxford, Oxford, OX1 3QU, UK

[d]School of Life Sciences & Department of Chemistry, University of Warwick, Coventry, CV4 7AL, UK

Running Head: Ethanol taxis in *Bacillus subtilis*.

#Address correspondence to Christopher V. Rao, cvrao@illinois.edu.

Payman Tohidifar, Girija A. Bodhankar, and Sichong Pei contributed equally to this work. Author order was determined on the basis of seniority.

Keywords: chemotaxis, *Bacillus subtilis,* ethanol sensing, cytoplasmic sensing

Abstract: 198 words; Importance: 121 words; Main Text: 5119 words

Abstract

Motile bacteria sense chemical gradients using chemoreceptors, which consist of distinct sensing and signaling domains. The general model is that the sensing domain binds the chemical and the signaling domain induces the tactic response. Here, we investigated the unconventional sensing mechanism for ethanol taxis in *Bacillus subtilis*. Ethanol and other short-chain alcohols are attractants for *B. subtilis*. Two chemoreceptors, McpB and HemAT, sense these alcohols. In the case of McpB, the signaling domain directly binds ethanol. We were further able to identify a single amino-acid residue Ala^{431} on the cytoplasmic signaling domain of McpB, that when mutated to a serine, reduces taxis to the alcohols. Molecular dynamics simulations suggest that mutation of Ala^{431} to serine increases coiled-coil packing within the signaling domain, thereby reducing the ability of ethanol to bind between the helices of the signaling domain. In the case of HemAT, the myoglobin-like sensing domain binds ethanol, likely between the helices encapsulating the heme group. Aside from being sensed by an unconventional mechanism, ethanol also differs from many other chemoattractants because it is not metabolized by *B. subtilis* and is toxic. We propose that *B. subtilis* uses ethanol and other short-chain alcohols to locate prey, namely alcohol-producing microorganisms.

Importance

Ethanol is a chemoattractant for *Bacillus subtilis* even though it is not metabolized and inhibits growth. *B. subtilis* likely uses ethanol to find ethanol-fermenting microorganisms for prey. Two chemoreceptors sense ethanol: HemAT and McpB. HemAT's myoglobin-like sensing domain directly binds ethanol, but the heme group is not involved. McpB is a transmembrane receptor consisting of an extracellular sensing domain and a cytoplasmic signaling domain. While most attractants bind the extracellular sensing domain, we found that ethanol directly binds between inter-monomer helices of the cytoplasmic signaling domain of McpB, using a mechanism akin to those identified in many mammalian ethanol-binding proteins. Our results indicate that the sensory repertoire of chemoreceptors extends beyond the sensing domain and can directly involve the signaling domain.

Introduction

Many bacteria move in response to external chemical gradients through a process known as chemotaxis (1). Typically, bacteria migrate up gradients of chemicals that support their growth and down ones that inhibit it. These chemicals are commonly sensed using transmembrane chemoreceptors, which consist of an extracellular sensing domain and a cytoplasmic signaling domain along with a cytoplasmic HAMP domain that couples the two domains. While a number of sensing mechanisms exist, the best understood one involves direct binding of the chemical to the extracellular sensing domain (2). In flagellated bacteria such as *Bacillus subtilis* and *Escherichia coli*, this binding event induces a conformational change in the cytoplasmic signaling domain that alters the autophosphorylation rate of an associated histidine kinase known as CheA (3). The phosphoryl group is then transferred to a soluble response regulator known as CheY, which modulates the swimming behavior of the bacterium by changing the direction of flagellar rotation. The chemical gradients themselves are sensed using a temporal mechanism involving sensory adaptation (4).

While many chemicals are sensed by the extracellular sensing domain, some are sensed by the cytoplasmic domains, typically using an indirect mechanism. For example, sugars transported by the phosphoenolpyruvate transfer system (PTS) are indirectly sensed through interactions between the PTS proteins and chemoreceptor signaling complexes (5, 6). In the case of *E. coli*, changes in intracellular pH are sensed by the cytoplasmic HAMP domain (7). The HAMP and the signaling domains of *E. coli* Tar are also responsible for the repellent response to nickel and an attractant response to toluene and *o*-xylene (8). In addition, changes in osmolarity are sensed through alterations in the

77 packing of the chemoreceptors cytoplasmic signaling domains (9). To our knowledge,
78 however, there have been no reports of direct sensing by the chemoreceptor cytoplasmic
79 signaling domain. This has not been particularly surprising given that the cytoplasmic
80 signaling domain, which consists of a long dimeric four-helix coiled-coil (10), lacks an
81 obvious ligand-binding pocket.

82 In this work, we investigated chemotaxis to ethanol in *B. subtilis*. This short-chain
83 alcohol is an attractant for *B. subtilis* even though it is not used as a carbon source and
84 inhibits cell growth. Ethanol is directly sensed by two chemoreceptors, HemAT and McpB.
85 Sensing by HemAT fits the conventional model where ethanol binds the sensing domain.
86 However, in the case of McpB, we found that ethanol is directly sensed by the cytoplasmic
87 signaling domain using a mechanism analogous to many eukaryotic ethanol-binding
88 proteins.

89

Results

***B. subtilis* exhibits chemotaxis to short-chain alcohols.** We employed the capillary assay to measure *B. subtilis* chemotaxis to alcohols with increasing chain lengths (C1 to C5). The resulting data show that *B. subtilis* exhibits chemotaxis to methanol, ethanol, 2-propanol, and *tert*-butanol. No significant responses to 1-propanol, 1-butanol, and 1-pentanol were observed (**Fig. 1A**). To elucidate the underlying sensing mechanism, we focused on ethanol, because it is produced and utilized by a wide range of microorganisms in nature (11). We first measured the response to increasing ethanol concentrations using the capillary assay. (**Fig. 1B**). Unlike many other attractants such as amino acids (12-14), a tactic response to ethanol was only observed at relatively high concentrations (> 50 mM). The ethanol response peaked at 1.78 M (~ 10% (v/v)). The response decreased at higher concentrations, most likely due to ethanol being toxic at these concentrations (15).

All three adaptation systems contribute to ethanol taxis. *B. subtilis* employs three adaptation systems – the methylation, CheC/CheD/CheYp, and CheV systems – for sensing chemical gradients (4, 16). To test whether these adaptation systems are involved in ethanol taxis, we employed mutants where these systems were selectively inactivated. We first tested ethanol taxis using a mutant (Δ*cheC* Δ*cheV*) where the CheC/CheD/CheYp and CheV adaptation systems were inactivated, leaving only the methylation system functional. Taxis to both ethanol and asparagine, which was used as a control, was reduced 30% in this mutant (**Fig. 1C**). We also observed reduced taxis in the Δ*cheC* and Δ*cheV* mutants, though the reduction was less than what was

observed with the double mutant. Interestingly, CheC/CheD/CheYp system appears to be more important for sensing ethanol gradients than for asparagine gradients (**Fig. 1C**). We did not test a Δ*cheR* Δ*cheB* mutant, which lacks the two enzymes involved in methylation system, because these mutants exhibit poor motility in general due to excessive tumbling.

McpB and HemAT are the chemoreceptors for short-chain alcohols. *B. subtilis* has ten chemoreceptors (17). To determine the chemoreceptors involved in ethanol taxis, we first tested mutants expressing just one chemoreceptor using the capillary assay. Only strains expressing McpB or HemAT as their sole chemoreceptor were capable of ethanol taxis (**Fig. 1D**). The response was greater for strains expressing HemAT, suggesting that it is the main receptor for ethanol taxis. This is not surprising as HemAT is more highly expressed than McpB (19,000 versus 6,200) (17). We next tested the effect of deleting these chemoreceptors in the wild type. When either McpB or HemAT was deleted (Δ*mcpB* or Δ*hemAT*), we observed reduced taxis toward ethanol. The reduction was greater in the Δ*hemAT* mutant, again suggesting that HemAT is the main receptor for ethanol taxis. When both chemoreceptors were deleted in the wild type (Δ*mcpB* Δ*hemAT*), ethanol taxis was almost completely eliminated while the mutant exhibited a normal response to proline, an amino-acid attractant for McpC (1138.7 ± 34.6 versus 1276.9 ± 54.1 of wild type) (**Fig. 1E**). We also found that strains expressing McpB or HemAT as their sole chemoreceptor responded to methanol, 2-propanol, and *tert*-butanol (**Fig. 1F**). Strains expressing HemAT as their sole

chemoreceptor exhibited stronger responses to these alcohols than strains expressing McpB alone with the exception of 2-propanol where the responses were similar.

Chemotaxis to ethanol is independent of its metabolism. Many bacteria metabolize ethanol (18). One possibility is that *B. subtilis* senses products of ethanol metabolism rather than ethanol itself. Indeed, such a mechanism occurs in *Pseudomonas putida* with regards to alcohol taxis (19). Therefore, we tested whether *B. subtilis* can grow on ethanol (**Fig. 2A**). These growth experiments were performed using the parental strain *B. subtilis* 168, which lacks the auxotrophies present in the chemotaxis strain OI1085. When cells were cultured in minimal medium with ethanol as the sole carbon source, no growth was observed. However, the cells did grow when ethanol was replaced with glucose. We also tested *B. subtilis* 168 growth in rich medium containing different amounts of ethanol to determine whether the cells were able to consume ethanol even though it does not support growth as the sole carbon source. While the cells were able to grow in rich medium containing ethanol, no decreases in ethanol concentrations were observed (**Fig. 2B**). These results indicate that *B. subtilis* does not consume ethanol.

Oxidation of alcohols to aldehydes and subsequently to carboxylic acids can potentially change the redox state of the cells. This change could possibly be perceived as a sensory signal through a process known as energy taxis (20). *B. subtilis* can ferment glucose to acetate and ethanol when grown in presence of pyruvate or a mixture of amino acids (21, 22). In this process, alcohol dehydrogenase (ADH) reduces acetaldehyde to ethanol using NADH as the cofactor. Whether ADH can oxidize ethanol

158 to acetaldehyde in *B. subtilis* is unknown. To test whether this occurs, we measured
159 ADH activities using *B. subtilis* cell lysates prepared from aerobic and anaerobic
160 cultures. As a positive control, ADH activities using *E. coli* cell lysates were also
161 measured (23). No ADH activity was observed with *B. subtilis* lysates whereas *E. coli*
162 lysates obtained from anaerobic cultures had an ADH activity of 31.25 ± 1.85 units/mL.
163 As expected, no ADH activity was detected with aerobic *E. coli* lysates. These results
164 suggest that ethanol taxis in *B. subtilis* is independent of ethanol catabolism and is
165 instead sensed directly by McpB and HemAT.
166
167 **Ethanol induces receptor-coupled kinase activity.** We next performed an *in vitro*
168 receptor-coupled kinase assay to test whether ethanol is able to activate CheA kinase
169 (24). This assay has been used to study how attractant binding to chemoreceptors
170 modulates CheA kinase activity (16, 24). Briefly, membranes expressing either McpB or
171 HemAT were isolated. The chemotaxis signaling proteins CheA, CheW, and CheD were
172 then added to these membranes to final concentrations that matched their stoichiometry
173 in wild-type cells. Using this assay, we found that ethanol activates CheA kinase in a
174 dose-dependent manner with membranes containing either McpB or HemAT as the sole
175 chemoreceptor. Ethanol concentrations as low as 10 mM were sufficient to activate CheA
176 kinase in both cases (**Fig. S1** and **Fig. 2C**). These results indicate that ethanol can induce
177 chemotaxis signaling *in vitro*. This assay, however, is unable to determine whether
178 ethanol directly interacts with the chemoreceptors, because the membranes might
179 contain associated proteins that could be involved in signaling.
180

McpB cytoplasmic signaling domain is involved in ethanol sensing. We next investigated ethanol taxis using receptor chimeras involving McpB to provide further insight regarding the sensing mechanism (25-27). We focused on McpB due to its high amino-acid similarity (57% to 65%) with three other *B. subtilis* chemoreceptors: McpA, TlpA, and TlpB. These four chemoreceptors all employ the same double Cache 1 domain for their sensing domain (2) and a highly conserved coiled-coil structure for their cytoplasmic signaling domain (10) (**Fig. 3A** and **3B**). Unlike McpB, HemAT is not a transmembrane chemoreceptor. We attempted to construct chimeras involving HemAT, McpA, and YfmS, another soluble chemoreceptor. However, none were functional in the sense that they did not respond to ethanol or molecular oxygen, which is the conventional attractant for HemAT (28).

We created chimeras between McpB and McpA, because the latter is not involved in ethanol taxis. In addition, we also measured the response to asparagine, because it is a known attractant for McpB, but not McpA, and binds the extracellular sensing domain (12). We first fused the N-terminal region of McpB to the C-terminal region of McpA: *mcpB*$_{287}$*A* and *mcpB*$_{359}$*A*. We then tested whether strains expressing these chimeras as their sole chemoreceptor respond to ethanol using the capillary assay. Both mutants did not respond to ethanol even though they still responded to asparagine (**Fig. 3C**). These results demonstrate that the extracellular sensing and cytoplasmic HAMP domains are not involved in sensing ethanol. Rather, the cytoplasmic signaling domain is involved. To verify our hypothesis, we tested a *mcpA*$_{358}$*B* chimera. As expected, a strain expressing *mcpA*$_{358}$*B* as its sole chemoreceptor responded to ethanol. This strain, however, does not respond to asparagine, because it lacks the requisite McpB sensing domain (**Fig. 3C**).

A key feature of chemoreceptor cytoplasmic signaling domains are the characteristic heptad repeats (labeled *a* to *g*) associated with their coiled-coil structure, where each repeat is equivalent to two helical turns. Based on sequence conservation and structural analysis of heptads from several bacterial and archaeal chemoreceptors, the cytoplasmic signaling domains are classified into three structurally distinct subdomains. These subdomains are known as the methylation (adaptation) helices, the flexible (coupling) bundle, and the conserved signaling tip (protein contact region) (10) (**Fig. 3** and **Fig. S2**). To narrow down the region on these subdomains involved in ethanol sensing, we created *mcpB*$_{374}$*A*, *mcpB*$_{397}$*A*, *mcpB*$_{423}$*A, mcpB*$_{433}$*A,* and *mcpB*$_{481}$*A* chimeras. Strains expressing *mcpB*$_{374}$*A* and *mcpB*$_{397}$*A* as their sole chemoreceptor did not respond to ethanol even though they still responded to asparagine. Strains expressing *mcpB*$_{423}$*A* as their sole chemoreceptor exhibited a reduced response to ethanol and asparagine. However, when *mcpB*$_{433}$*A* and *mcpB*$_{481}$*A* were tested, the corresponding chimera expressing strains were able to respond to ethanol and asparagine at levels similar to the wild-type control (**Fig. 3C**). These results suggest that the region spanning the residues 397 to 433 on McpB is involved in sensing ethanol. Furthermore, the region spanning the residues 423 to 433 on McpB appears to be the principal region involved in ethanol sensing.

McpB residue involved in ethanol sensing. The region spanning residues 397 to 433 on McpB is necessary for ethanol taxis. As a first step towards identifying the binding site, we performed *in silico* docking experiments with ethanol and the McpB dimer fragment spanning residues 390 to 435 on the N-helix and neighboring residues 577 to 622 on the C-helix. The resulting data from the docking analysis yielded five distinct

clusters of putative amino acid residues involving both the N-helix and the C-helix of the dimer fragment (**Table S1** and **Fig. S3A**). We next aligned the amino-acid sequences spanning residues 392 to 434 on the N-helix and neighboring residues 578 to 620 on the C-helix of McpB, McpA, TlpA, and TlpB. (**Fig. S3B**). Among the 20 putative binding residues, Thr^{424}, Asp^{427}, and Ala^{431} on the N- helix and Glu^{581} and Lys^{585} on the C-helix were not conserved between the four chemoreceptors and, thus, were targeted for mutational analysis (**Fig. 4A** and **4B**). Mutants expressing *mcpB-T424A, mcpB-D427T, mcpB-E581Q,* and *mcpB-K585E* as their sole chemoreceptor exhibited responses to ethanol similar to the wild-type *mcpB*. However, the strain expressing *mcpB-A431S* as its sole chemoreceptor failed to respond to ethanol. In addition, all strains supported asparagine taxis*,* indicating that these mutated receptors were functional (**Fig. 4C**)*.* We also measured the response of the strain expressing *mcpB-A431S* to methanol, 2-proponal, and *tert*-butanol in the capillary assay and observed reduced responses (**Fig. 4D**), suggesting that Ala^{431} is an important residue for alcohol taxis overall.

Ethanol directly binds to the McpB cytoplasmic signaling domain. To test whether ethanol directly interacts with McpB, we conducted saturation-transfer difference nuclear magnetic resonance (STD-NMR) experiments using recombinant McpB. STD-NMR has been used to measure weak interactions between proteins and their ligands (29-32). Briefly, in these experiments, the protein is selectively saturated at specific frequencies. The magnetization is then transferred to the surrounding, low molecular-weight ligands in a distance-dependent manner. The ligand epitopes in close proximity of the protein receive higher saturation (33), implying direct binding to the protein.

We first tested the McpB cytoplasmic region ($McpB_C$) spanning residues 305 to 662, which corresponds to the HAMP and signaling domains (see **Fig. 3A**). The resulting ^1H spectra for the $McpB_C$ protein incubated with 3 mM ethanol (60-fold excess of the protein) is shown in **Fig. 4E**. Two peaks for ethanol appeared near 1.05 ppm and 3.51 ppm, which respectively correspond to $-CH_3$ and $-CH_2$ epitopes of ethanol. Ligand signals were also observed at the expected chemical shift values (1.05 ppm and 3.51 ppm) on the STD spectra. Additionally, the area under the STD peak corresponding to the $-CH_2$ epitope was about five-fold (18%) less than that of the $-CH_3$ epitope (**Fig. 4E**), suggesting that the $-CH_3$ moiety of ethanol is closer to the protein than its $-CH_2$ moiety. Moreover, control experiments using 3 mM 1-pentanol, which is not an attractant, and McpBc showed negligible STD peaks near the characteristic chemical shift values (3.5, 1.41, 1.18, 0.8 ppm), suggesting that 1-pentanol does not bind McpBc (**Fig. S4A**). As an additional negative control, we performed STD-NMR experiments using the McpA cytoplasmic region spanning residues 305 to 661 with 3 mM ethanol. Consistent with our *in vivo* results, we did not observe significant STD peaks near the characteristic chemical shift values (**Fig. S4A**). These results collectively indicate that ethanol directly interacts with the McpB cytoplasmic region.

Strains expressing *mcpB*-A431S as their sole chemoreceptor exhibited a reduced response to ethanol when tested in the capillary assay (**Fig. 4C**). To determine whether the A431S mutation reduces ethanol binding, we repeated the STD-NMR experiments with recombinant $McpB_C$-A431S protein. Because single mutations may impair proper folding of proteins, we first measured the circular dichroism spectra for both the wild-type $McpB_C$ and the $McpB_C$-A431S proteins. We observed similar spectra for both proteins,

which suggests that the mutant protein preserves the wild-type helical structure (**Fig. S4**). We then performed STD-NMR experiments with the $McpB_C$-A431S in presence of 3 mM ethanol. The resulting STD spectra showed reduced peaks near 1.05 ppm and 3.51 ppm as compared to wild-type $McpB_C$ (**Fig. 4E**). The saturation fraction of ethanol, which corresponds to the ratio of areas under the respective -CH_3 peaks on STD and ^1H spectra, is 0.23 for $McpB_C$ and 0.1 for the $McpB_C$-A431S. These results imply that the residue Ala^{431} has a role in ethanol binding to the McpB signaling domain.

Molecular dynamics simulation suggests the A431S mutation reduces ethanol affinity to the McpB cytoplasmic signaling domain. To gain insight regarding the ethanol binding mechanism, we performed molecular dynamics simulations of the wild-type and A431S McpB cytoplasmic signaling dimers (residues 352 to 662) in presence of ethanol. Our simulations demonstrate that ethanol can bind nonspecifically throughout the cytoplasmic signaling domain in both the wild-type and the mutant McpB dimers, primarily interacting along the inter-helical grooves of the four-helix bundle (**Fig. 4F** and **Fig. S5A**). A comparison of the ethanol occupancy between the wild-type and A431S mutant McpB shows little variation overall but exhibits a marked difference in the region immediately surrounding residue 431. In particular, while ethanol was observed to bind at both the inter- and intra-monomer interfaces in the wild-type simulations, the inter-monomer binding site associated with the residue 431 side chain was not present in the mutant simulations (**Fig. 4G),** suggesting that the A431S mutation reduces the binding affinity of ethanol. Indeed, within the flexible-bundle region, the residues displaying the greatest change in ethanol coordination between the wild-type and the A431S mutant

296 form a concentric pocket centered on residue 431 at the inter-monomer interface (**Fig.**
297 **4H**).

298 Our analyses identified another interesting feature of ethanol binding, namely that it is
299 able to penetrate the surface of the McpB cytoplasmic domain to bind within the core of
300 the coiled coil. In particular, we observed that ethanol entered between the individual
301 helices of the four-helix bundle at two locations in the methylation-helix region: one
302 involving N-helix residues 393-400 and C-helix residues 613-617 and another involving
303 N-helix residues 382-387 and C-helix residues 628-631 (**Fig. S5A**). While ethanol binding
304 to these regions was observed in both the wild-type and A431S mutant simulations, the
305 wild-type binding events resulted in longer dwell times, giving rise to the difference in
306 ethanol coordination observed in these regions (**Fig. S5A**). Preliminary analysis of the
307 two sites, however, suggests they do not themselves play a significant role in signaling.
308 The latter is located outside the region involved in ethanol sensing (see **Fig. 3C**) and the
309 former, except for residue Glu^{399}, is highly conserved among the four chemoreceptors
310 (see **Fig. S3B**). Indeed, we did not observe a significant reduction in response to ethanol
311 compared to the wild-type control when we tested a mutant expressing *mcpB-E399K* as
312 its sole chemoreceptor in the capillary assay (569 ± 29.1 cells versus 586.1 ± 9.0 cells,
313 respectively). Nevertheless, these observations hint at a signaling mechanism in which
314 ethanol may penetrate to the core of the cytoplasmic domain where it can affect the
315 packing and overall stability of the bundle.

316 To further investigate the above packing hypothesis, we analyzed the strength of
317 knobs-in-holes interactions in the region surrounding residue 431 over the course of the
318 simulations. We observed that the A431S mutation leads to increased occupancy of the

431 knob itself as well as nearby knobs on the C-helix at positions 583 and 585 (**Fig. S5B**), indicating stronger hydrophobic interactions between the individual helices. Therefore, our simulation results suggest that the A431S mutation, which decreases the McpB ethanol response, not only reduces the direct binding of ethanol but also strengthens coiled-coil packing in the region. One possibility is that the reduced local concentration of ethanol and improved packing in the A431S mutant decreases the ability of ethanol to intercalate with the knobs-into-holes interactions near residue 431 and, thus, its ability to induce signaling.

The HemAT sensing domain helices are involved in direct ethanol sensing. HemAT is a cytoplasmic chemoreceptor, which consists of an N-terminal sensing domain and a C-terminal signaling domain. To determine whether the HemAT signaling domain is also involved in ethanol sensing, we conducted the STD-NMR experiments with the purified signaling domain ($HemAT_S$), spanning residues 177 to 432, and the purified sensing domain ($HemAT_N$), spanning residues 1 to 178 of the HemAT, in presence of 3 mM ethanol. The STD spectra with the HemAT signaling domain showed negligible peaks near the expected chemical shift values (1.05 ppm and 3.51 ppm) while the resulting ^1H and STD spectra with the $HemAT_N$ showed clear peaks near 1.05 ppm and 3.51 ppm, which correspond to the $-CH_3$ and the $-CH_2$ moieties of ethanol. The ratio of areas in the STD spectra compared to ^1H spectra was 0.27 for the $-CH_3$ moiety and 0.85 for the $-CH_2$ moiety, suggesting that $-CH_2$ moiety of ethanol is closer to the protein than its $-CH_3$ moiety. (**Fig. 5A**). These results collectively indicate that ethanol binds the sensing domain of the HemAT.

342 The sensing domain of the HemAT dimer is composed of a four-helical bundle as its
343 core and a heme group in each subunit (**Fig. 5B**), which is known to bind molecular
344 oxygen (34). UV-spectral analyses have shown that the oxygen molecule binds the heme
345 group by forming hydrogen bonds with 6-coordinate ferrous heme (35, 36). To determine
346 whether the heme group also interacts with ethanol, we conducted UV spectroscopy
347 experiments with the purified HemAT sensing domain ($HemAT_N$) and ethanol. As a
348 control, we first measured UV absorption of both oxygenated and deoxygenated forms of
349 the protein to verify that the heme group on the purified protein is functional. Consistent
350 with the previous reports (28, 35, 37), the oxygenated form of the $HemAT_N$ exhibited three
351 major canonical peaks at 412 nm (Soret), 544 nm (β-band), and 578 nm (α-band), and
352 the dithionite-reduced deoxygenated form of the protein exhibited two major peaks at 434
353 nm and 556 nm (**Fig. 5C**). Next, we measured UV absorption of the deoxygenated
354 HemAT sensing domain in presence of varying concentrations of ethanol. The resulting
355 spectra showed two major peaks at 434 nm and 556 nm similar to what we observed with
356 the deoxygenated form of the protein in absence of any ligand (**Fig. 5C**). These results
357 imply that the heme group does not interact with ethanol. Rather, they suggest that
358 ethanol binds the alpha helices of the HemAT sensing domain, perhaps using a
359 mechanism similar to the one proposed for the McpB cytoplasmic signaling domain.
360

Discussion

We found that *B. subtilis* performs chemotaxis to multiple short-chain alcohols. These alcohols are directly sensed by two chemoreceptors, McpB and HemAT. McpB is a transmembrane chemoreceptor, with an extracellular sensing domain and a cytoplasmic signaling domain, linked by a cytoplasmic HAMP domain. It is known to sense the amino-acid asparagine and alkaline environments as attractants using the extracellular sensing domain (12, 25). HemAT, on the other hand, is a soluble chemoreceptor, which consists of a sensing and signaling domain but lacks a HAMP domain. Its myoglobin-like sensing domain contains heme and is known to bind molecular oxygen (28, 36). Using chimeric receptors and STD-NMR, we found that short-chain alcohols are directly sensed by the cytoplasmic signaling domain of McpB and the sensing domain of HemAT. In the case of HemAT, the alcohols do not appear to bind heme; rather, they likely bind between the helices encapsulating the heme.

Among the alcohols tested, ethanol is the most likely physiological attractant, because it is produced by many microorganisms and is prevalent in nature (11). As a consequence, we focused on this chemical. Curiously, ethanol is not consumed by *B. subtilis*, suggesting that it is used for purposes other than nutrition. One possibility is that *B. subtilis* uses ethanol to locate prey, which could potentially explain why *B. subtilis* is attracted to a chemical that nominally inhibits its growth. The most likely prey are Crabtree-positive yeast such as *Saccharomyces cerevisiae*, which produce ethanol at high concentrations even during aerobic growth (38). Indeed, *B. subtilis* can lyse *S. cerevisiae* cells through the production of cell-wall degrading compounds (**Fig. S6**) (39-41).

Aside from ethanol, methanol may also be a physiological attractant. It is a byproduct of pectin degradation and, as a consequence, can contaminate alcoholic beverages (42). However, *B. subtilis* does not consume methanol because it lacks methanol dehydrogenase activity (43). Similar to ethanol, *B. subtilis* may use methanol to locate prey, this time pectin-degrading microorganisms.

These speculations are in line with the results from an earlier study where no correlation was observed between the metabolic and chemotactic preferences of *B. subtilis* for amino acids. This study proposed that *B. subtilis* uses amino-acid gradients as cues to locate sources of nutrients, for example, during plant root colonization (44, 45). The only other bacterium known to exhibit taxis toward alcohols is *Pseudomonas putida* (19). However, this bacterium consumes alcohols. In addition, it does not directly sense these alcohols but rather the byproducts of their degradation, namely carboxylic acid. Finally, alcohol taxis is also observed in *E. coli* and *Ralstonia pseudosolanacearum*. In these bacteria, however, alcohols are sensed as repellents (46, 47).

A key difference between taxis to alcohols and conventional attractants, such as amino acids, is their respective sensitivities. Amino acids are sensed at micromolar concentrations whereas alcohols are sensed at millimolar concentrations. Though it should be noted while low millimolar concentrations (e.g. 3 mM) of ethanol can bind McpB and HemAT *in vitro*, much higher ethanol levels are required for optimal chemotaxis in the capillary assay experiments. The disparity may be due to the architecture of the capillary assay. Briefly, chemotaxis to ethanol occurs when ethanol concentrations in the capillaries are as low as 50 mM (190.1 ± 44.5 cells versus 42.3 ± 6.2 cells for buffer) and the response to ethanol peaks when capillaries contain about 2 M ethanol. These

concentrations, however, do not reflect the ethanol concentrations that cells experience near mouth of the capillary in the pond. Three-dimensional simulations based on finite-element analysis of ethanol diffusion from a capillary into a pond indicate that ethanol concentration falls dramatically, 10-50 times as compared with initial ethanol concentration in the capillary near mouth of the capillary (**Fig. S7**). These simulation results suggest that cells are able to respond to ethanol levels ranging from 1 – 200 mM. That said, the weak affinity for alcohols is not surprising as most ethanol receptors in mammals also exhibit weak affinity for ethanol (48).

The question then is whether ethanol is actually an attractant for *B. subtilis* given that relatively high concentrations are necessary to elicit taxis. Over-ripe fruits provide one potential source for high ethanol concentrations, where concentrations can exceed one molar (49). In addition, flooded plant roots can also provide another source at millimolar concentrations (50-52). In this case, *B. subtilis* perhaps uses ethanol to locate roots for colonization to initiate symbiosis (44). This suggests that ethanol taxis can indeed occur in the environment. Whether the other alcohols reach such concentrations in the environment is not known.

Perhaps the most interesting aspect of ethanol taxis involves the sensing mechanism. Typically, small-molecule attractants bind the extracellular sensing domain. The main exceptions are PTS sugars, which are sensed indirectly through the PTS system (5, 6). Ethanol is sensed intracellularly. In the case of HemAT, this distinction is minor, as ethanol binds the sensing domain, albeit one normally associated with oxygen sensing. In the case of McpB, the cytoplasmic signaling domain is involved in sensing ethanol through direct binding. This appears to be first documented case of the cytoplasmic

signaling domain being directly involved in sensing. While we were able to establish that ethanol binds the McpB cytoplasmic signaling domain using genetics and STD-NMR, the detailed binding and induced signaling mechanisms are still somewhat opaque. In particular, it is not clear whether ethanol exerts its effect precisely at residue 431 or possibly at one or multiple other positions along the lengthy cytoplasmic domain. Molecular dynamics simulations suggest that ethanol can bind nonspecifically at several places on the McpB cytoplasmic surface as well as penetrate to the core of the four-helix bundle, at least within the methylation helix region. Although we did not observe ethanol enter the bundle core near residue 431 in our simulations, it may do so on longer timescales or in particular signaling states. In addition, the precise molecular details of how ethanol binding induces signaling in wild-type McpB remain to be worked out. The enhanced packing interactions in the A431S McpB, which does not respond to ethanol, suggest that it may disrupt or loosen packing, leading to changes in the overall stability of McpB that can be transmitted to the kinase. This idea is in line with numerous previous studies of the *E. coli* Tsr and Tar chemoreceptors, for example, that suggest that changes in the periplasmic ligand binding and adaptation state affect packing throughout the cytoplasmic bundle (5, 6).

Many aspects of ethanol sensing in *B. subtilis* are analogous to mechanisms observed in higher eukaryotes. Alcohols generally bind proteins with low affinities, and relatively high concentrations of alcohols are required to induce behavioral effects. For example, ligand-gated ion channels receptors such as the N-methyl-D-aspartate-type glutamate receptors, γ-aminobutyric acid type A ($GABA_A$) receptors, and glycine receptors all exhibit weak affinity for ethanol (> 10 mM) (48). Although the binding sites on these proteins are

not well characterized, ethanol is thought to bind helical regions in most cases. In the case of $GABA_A$ receptor, for example, ethanol binds within a small cavity between two transmembrane helices (TM2 and TM3) (53). Molecular dynamics studies show that ethanol modulates the receptor states by stabilizing helical crossing angles with a 'wringing motion' (54, 55). Ethanol inhibition of the NMDA receptor is regulated by counteracting forces on M3 helices of the receptors with additional interactions with side chains (56). Potassium channels are also affected by >100 mM ethanol concentrations. Kinetic and structural studies of Shaw2 K^+ channels have shown that the alpha helical propensity of the loop in the pore forming subunit is important for ethanol binding (57) . Similarly, in the case of odorant binding protein LUSH from *Drosophila melanogaster*, a small cavity between the alpha helices accommodate a single ethanol molecule, where its hydroxyl group form hydrogen bonds with neighboring Thr^{57} and Ser^{52} residues (58). The binding motif found in LUSH is shared by the $GABA_A$-R receptor, glycine receptor and *Drosophila* Shaw2 K^+ channel (58), suggesting a common alcohol-binding mechanism in eukaryotes. Experimental and computational studies of the ion channel GLIC in the bacterium *Gloeobacter violaceus* also point to a mechanism of alcohol binding within cavities between transmembrane helices (59). Analysis of binding sites from structural studies suggests that ethanol preferentially binds helices with amphipathic surfaces (48, 60, 61). The sensing mechanisms for these proteins typically involve replacement of water molecules with ethanol within small hydrophobic cavities between two or more helices. Indeed, an analogous mechanism appears to be employed by the *B. subtilis* chemoreceptors. Given the reported similarities in the mode of action of ethanol

474 in both prokaryotic and eukaryotic proteins, the model hypothesized in this investigation
475 could provide evolutionary clues on the mechanisms of alcohol sensing proteins.
476
477

Materials and Methods

Chemicals and growth media. The following media were used for cell growth: Luria-Bertani broth (LB: 1% tryptone, 0.5% yeast extract, and 0.5% NaCl); tryptone broth (TB: 1% tryptone and 0.5% NaCl); tryptose blood agar base (TBAB: 1% tryptone, 0.3% beef extract, 0.5% NaCl, and 1.5% agar); yeast-peptone-dextrose broth (YPD: 1% yeast extract, 2% peptone, and 2% dextrose); and capillary assay minimal medium (CAMM: 50 mM potassium phosphate buffer (pH 7.0), 1.2 mM $MgCl_2$, 0.14 mM $CaCl_2$, 1 mM $(NH_4)_2SO_4$, 0.01 mM $MnCl_2$, and 42 μM ferric citrate). Chemotaxis buffer consists of 10 mM potassium phosphate buffer (pH 7.0), 0.14 mM $CaCl_2$, 0.3 mM $(NH_4)_2SO_4$, 0.1 mM EDTA, 5 mM sodium lactate, and 0.05% (v/v) glycerol. All alcohols used in this study were purchased from Fisher Scientific, Inc.

Strains and plasmids. All strains and plasmids used in this work are listed in Tables 1 and 2, respectively. Chemotaxis experiments were performed with derivatives of *B. subtilis* OI1085. Growth experiments were performed using *B. subtilis* 168, which is the parental strain. The undomesticated *B. subtilis* strain NCBI3610 and the *Saccharomyces cerevisiae* CEN.PK113-7D yeast strain were used in the antimicrobial diffusion assays. All cloning was performed using NEB® 5-alpha Competent *E. coli* (New England Biolabs). All oligonucleotides used in this study are provided in (**Table S2**).

Gene deletions were constructed using plasmids derived from pJSpe, which provides a CRISPR/Cas9-based, marker-free, and scarless genome editing system for *B. subtilis* (62). To construct a deletion vector, a 20-bp crRNA target sequence complementary to the targeted gene sequence was designed using the CHOPCHOP online tool (63). The

5’-end phosphorylated complementary oligonucleotides were then annealed and subcloned into BsaI restriction sites on pJSpe plasmid using Golden Gate assembly (64). The resultant plasmid was then linearized at SpeI restriction site and joined to two PCR fragments (~700 to 800 bp) flanking the targeted gene using Gibson assembly (65). Prior to transformation into *B. subtilis* strain, each of the pJSpe-derived deletion plasmids was linearized at XhoI restriction site and subsequently self-ligated to create a long DNA concatemer. The concatemer was then transformed into *B. subtilis* strain using the two-step Spizizen method (66). Transformation product of *B. subtilis* strain and deletion plasmid concatemer was incubated on a LB agar (LB and 1.5% agar) plate supplemented with 5 µg/mL kanamycin and 0.2% mannose for about 24 h at 30 °C. Next, single colonies were isolated and twice streaked on fresh drug plates (described above) to assure a clonal genotype. Positive colonies were verified using colony PCR and again streaked on a plain LB agar plate and incubated for additional 24 h at 50 °C to cure the deletion plasmid. Colonies with cured plasmids were unable to grow on a LB agar plate supplemented with 5 µg/mL kanamycin.

To construct chemoreceptor chimeras, two opposing primers were designed to amplify DNA regions outward from the fusion points of the chimeric gene using PCR with pAIN750*mcpB* integration plasmid as the DNA template. Then, a second pair of primers with short overlapping regions were used to PCR amplify the desired fragment of *mcpA* gene from pAIN750*mcpA*. Following purification of PCR DNA products by gel extraction, the DNA fragments were assembled using Gibson assembly and transformed into *E. coli*. Following isolation from *E. coli* and sequence verification, the concatemer of the resultant integration plasmid was prepared as described above and transformed into *B. subtilis*

OI3545, which lacks all ten chemoreceptors. Transformation product was then incubated on a LB agar plate supplemented with 100 μg/mL spectinomycin for 15 h at 37 °C. Single colonies were isolated and streaked on a TBAB agar (TBAB and 1.5% agar) plate supplemented with 1% soluble starch. A single positive colony with chemoreceptor expression cassette recombined to *amyE* locus was verified using Gram Iodine solution (0.33% iodine, 0.66% potassium iodide, and 1% sodium bicarbonate). Correct colonies with disrupted *amyE* gene were unable to form clear zones on TBAB-starch plate.

Point mutations on *mcpB* chemoreceptor gene were introduced using the inverse PCR method. Briefly, two opposing primers containing the desired mutations were used to PCR amplify integration pAIN750*mcpB* plasmid. Following purification of PCR DNA by gel extraction, 5'-ends of the DNA fragment was phosphorylated with T4 polynucleotide kinase and then blunt-end ligated using T4 DNA ligase. Ligation product was heat-inactivated and transformed into *E. coli*. Following isolation from *E. coli* and sequence verification, concatemer of the resultant integration plasmid was prepared as described above and transformed into *B. subtilis* OI3545 to integrate the mutant chemoreceptor expression cassette into the *amyE* locus.

Protein expression plasmids were constructed with the pET28(+) expression vector system using Gibson assembly. Briefly, DNA for the HemAT sensing domain (residues 1 to 178) was cloned in frame with a C-terminal His_6-tag between the NcoI and HindIII restriction sites on pET28a(+). Similarly, the DNAs for the wild-type McpB, wild-type McpA and McpB[A431S] cytoplasmic regions including the HAMP domain (residues 305 to 662 for McpB and residues 304 to 661 for McpA) were cloned in frame with a C-terminal His_6 tag at NcoI restriction site on pET28a(+). The DNA for HemAT signaling domain (residues

547 177 to 432) was cloned in frame with a N-terminal His_6-tag at the NheI restriction site on
548 pET28a(+). After isolation and sequence verification, all plasmids were transformed into
549 *E. coli* BL21 (DE3) strain for protein expression and purification.
550
551 **Protein expression and purification.** CheA, CheW, and CheD proteins used in the
552 kinase assay were expressed from glutathione *S*-transferase (GST) fusion plasmids and
553 purified from *E. coli* BL21(DE3) strain as described previously (16, 24). GSTrap columns
554 (5 mL; GE Healthcare) were used with an Akta Prime FPLC system (GE Healthcare) for
555 purification. To purify the GST fusion proteins, cells were grown in 2 liters of LB with 100
556 µg/mL ampicillin at 37 °C and shaking at 250 rpm until OD_{600} = 0.8. Expression was then
557 induced by the addition of 1 mM IPTG (isopropyl-β-d-thiogalactopyranoside), and the
558 culture was grown for 12 h at 25 °C with 250 rpm shaking. For CheA, the culture was
559 induced at 37 °C for 4 h. Cells were then centrifugated at 8000 x *g* for 8 min and
560 resuspended in Tris-buffered saline (TBS: 50 mM Tris, 150 mM NaCl, pH 7.5)
561 supplemented with 1% Triton X100 and 1 mM of dithiothreitol (DTT) for every 1 g of cell
562 pellet. The cells were then disrupted by sonication (5 x 10 s pulse). The supernatants
563 were clarified by two rounds of centrifugations (9,000 x *g*, 15 min; 40,000 x *g*, 40 min),
564 and loaded onto 5 mL GSTrap columns pre-washed with 10 column-volumes of TBS.
565 Protein-bound columns were then washed with at least 15 volumes of TBS, and GST
566 tagged proteins were eluted using 10 mL glutathione elution buffer (GEB: 50 mM Tris, 5
567 mM glutathione, pH 8). To remove the GST tag, the purified proteins were cleaved by
568 PreScission protease, as specified by the supplier (Amersham Biosciences), and applied
569 to another 5 mL GSTrap column. The flow-through was collected and concentrated to

570 approximately 5 mL using a cellulose ultrafiltration membrane (Millipore) in an Amicon
571 ultrafiltration cell. Last, the purified proteins were dialysed in TKMD buffer (50 mM Tris,
572 50 mM KCl, 5 mM $MgCl_2$, 0.1 mM DTT, pH 8) and aliquots were stored at −80°C.
573 *E. coli* BL21 (DE3) cells harboring the His_6-tagged expression plasmids were grown
574 in 2 L of LB medium supplemented with 30 µg/mL kanamycin at 37 °C and shaking at 250
575 rpm until A_{600} = 0.7. Expression was then induced by the addition of 1 mM IPTG, and the
576 cultures were grown for 12 h at 25 °C. Cells were harvested by centrifugation at 7,000 x
577 *g* at 4°C for 10 min. Cells harboring $HemAT_N$ were resuspended in lysis buffer (50 mM
578 NaH_2PO_4, 300 mM NaCl, 10 mM Imidazole, pH 8) and sonicated (5 x 10 s pulses). Cell
579 debris was removed by centrifugation at 12,000 x *g* for 1 h. The dark-red supernatant
580 containing $HemAT_N$ was loaded on a 5 mL GE HisTrap column prewashed with $NiSO_4$
581 and binding buffer (50 mM NaH_2PO_4, 300 mM NaCl, 20 mM imidazole, pH 8). The protein-
582 bound column was then washed with binding buffer and proteins were eluted with elution
583 buffer (50 mM NaH_2PO_4, 300 mM NaCl, 250 mM Imidazole, pH 8). The collected $HemAT_N$
584 protein samples were concentrated using an Amicon ultrafiltration cell (Millipore) and
585 dialyzed into dialysis buffer (50 mM Tris, 300 mM NaCl, pH 8) at 4 °C and aliquots were
586 stored at -80°C.
587 $McpB_C$, $McpB_C$ [A431S], $McpA_C$, and $HemAT_S$ proteins were purified under denaturing
588 conditions. Briefly, cells were induced and grown as described above. Cells were then
589 resuspended in buffer B (8 M urea, 0.1 M NaH_2PO_4, 0.01 M Tris, pH 8) with 1% Triton
590 X100 and 1 mM of DTT for every 1 g of cell pellet and incubated at room temperature for
591 1 h. Cell suspension was clarified by centrifugation at 40,000 x *g* for 1 h. The cell lysates
592 were loaded onto 5 mL GE Hi-Trap Chelating column charged with 0.1 M $NiSO_4$ and

593 washed with buffer B and buffer C (buffer B at pH 6.3). The fusion proteins were eluted
594 from the column with 25 mL elution buffer E (buffer B at pH 4.5). Proteins were refolded
595 by dialyzing in PBS (10 mM Na_2HPO_4, 1.8 mM KH_2PO_4, 137 mM NaCl, 2.7 mM KCl, pH
596 7.4) at 4 °C, and aliquots were stored at -80 °C. Purified proteins proper folding was
597 verified with circular dichroism spectroscopy. Concentration of all purified proteins were
598 quantified by Pierce BCA protein assay kit. SDS-PAGE images of the purified
599 recombinant chemoreceptor proteins are shown in Data set S1.
600
601 **Capillary assay for chemotaxis.** The capillary assay was performed as described
602 previously (67). Briefly, cells were grown for 16 h at 30 °C on TBAB plates. The cells were
603 then scraped from the plates and resuspended to OD_{600} = 0.03 in 5-mL CAMM
604 supplemented with 50 µg/mL histidine, 50 µg/mL methionine, 50 µg/mL tryptophan, and
605 20 mM sorbitol, and 2% TB. The cultures were grown to OD_{600} = 0.4 – 0.45 at 37 °C with
606 shaking at 250 rpm. At this point, 50 µL of GL solution (5% (v/v) glycerol and 0.5 M sodium
607 lactate) was added, and cells were incubated for another 15 min (at 37 °C and 250 rpm
608 shaking). The cells were then washed twice with chemotaxis buffer and incubated for
609 additional 25 min (at 37 °C and 250 rpm shaking) to assure that the cells were motile.
610 Cells were then diluted to OD_{600} = 0.001 in chemotaxis buffer and aliquoted into 0.3-mL
611 ponds on a slide warmer at 37 °C and closed-end capillary tubes filled with alcohol
612 solutions or asparagine solution (3.16 µM) prepared in the same chemotaxis buffer were
613 inserted. After 30 min, cells in the capillaries were harvested and transferred to 3 mL of
614 top agar (1% tryptone, 0.8% NaCl, 0.8% agar, and 0.5 mM EDTA) and plated onto TB
615 agar (TB and 1.5% agar) plates. These plates were incubated for 16 h at 37 °C and

colonies were counted. Experiments were performed in triplicate each day and repeated on three different days.

Cell growth. Cells density was measured as optical absorbance at 600 nm. Briefly, *B. subtilis* 168 was first grown for 16 h at 30°C on a TBAB plate. For growth experiments in minimal medium, the cells were first scraped from the TBAB plate and then resuspended to OD_{600} = 0.03 in 50 mL CAMM supplemented with 50 µg/mL tryptophan and 5 g/L glucose; and grown at 37 °C with shaking at 250 rpm. At the OD_{600} = 0.8, the cells were diluted 1:20 (v/v) into 50 mL CAMM containing 50 µg/mL tryptophan, supplemented with 0.01 M ethanol, 0.1 M ethanol, or 5 g/L glucose (positive control), respectively, and grown for 24 h at 37 °C with shaking at 250 rpm. For growth experiments in rich medium, cell cultures starting at OD_{600}=0.03 were grown to OD_{600} = 0.4 at 37°C with shaking at 250 rpm in 50 mL LB media. At this point, cell cultures were supplemented with 0.01 M, 0.1 M, or 1.0 M ethanol, respectively, and grown for another 5 h at 37°C with shaking at 250 rpm. All growth experiments were performed in triplicate.

Ethanol utilization experiments. Ethanol concentrations were measured using a Shimadzu high-performance liquid chromatography system equipped with a RID-10A refractive index detector, an Aminex HPX-87H carbohydrate analysis column (Bio-Rad Laboratories), and a cation H microguard cartridge (Bio-Rad Laboratories). The column and guard cartridge were kept at 65 °C, and 0.5 mM H_2SO_4 was used a mobile phase at a constant flow rate of 0.6 mL/min. Prior to measurements, cells in culture samples were pelleted, and the resulting supernatant was passed through a 0.22-µm polyethersulfone

639 syringe filter. Peaks were identified and quantified by retention time comparison to the
640 standards.
641
642 **Alcohol dehydrogenase activity measurement.** *B. subtilis* OI1085 was first grown
643 for 16 h at 30 °C on a TBAB plate. For aerobic growth, the cells were then scraped from
644 the TBAB plate and resuspended to OD_{600} = 0.03 in 5 mL CAMM supplemented with 50
645 µg/mL histidine, methionine, tryptophan, 20 mM sorbitol, and 2% TB, and grown at 37 °C
646 with vigorous shaking at 250 rpm. For anaerobic growth, however, cells were cultured
647 starting at OD_{600} = 0.03 in a sealed bottle filled to the top without agitation in CAMM
648 supplemented with 1% glucose and mixture of all 20 amino acids at 50 µg/mL (21). For
649 *E. coli* cultures, the cells (MG1655) were grown in M9 media supplemented with 0.4%
650 glucose at 37°C in sealed bottles filled to the top without agitation for anaerobic growth
651 and in flasks with shaking at 250 rpm for aerobic growth (23). All cell cultures were grown
652 to stationary phase prior to sonication (7 x 10 s pulses), and soluble cell extracts were
653 obtained by centrifugation (7000 x *g* at 4°C for 10 min). Alcohol dehydrogenase enzyme
654 assays were performed as described previously (68). Briefly, the assay reactions were
655 prepared with 22 mM sodium pyrophosphate (pH 8.8), 0.3 mM sodium phosphate, 7.5
656 mM β-nicotinamide adenine dinucleotide, 0.003% (w/v) bovine serum albumin, 1.6% (v/v)
657 of desired cell lysate, and 3.2% (v/v) ethanol in 200 µL reaction volume. Then, the
658 reduction of NAD^+ to NADH was recorded at 340 nm using a Shimadzu UV-1800
659 spectrophotometer. One unit of alcohol dehydrogenase activity is defined as the amount
660 of enzyme that converts 1 µmole of ethanol to acetaldehyde per minute at pH 8.8 at 25
661 °C.

662

663 **Antimicrobial diffusion assay.** Antifungal activity of the *B. subtilis* strains were
664 assayed using the disc diffusion method as described previously (69). Briefly, the *S.*
665 *cerevisiae* CEN.PK113-7D was grown in YPD rich medium for 24 h at 30 °C with shaking
666 at 200 rpm. 0.1% (v/v) of yeast culture was mixed with YPD top agar (YPD with 0.8%
667 agar) and spread on top of a YPD plate (YPD with 2% agar). Once top yeast layer was
668 solidified, 10-mm filter paper (Whatman Filter Paper, Grade 1) discs loaded with
669 supernatants from *B. subtilis* strains grown overnight in LB medium at 37°C, were placed
670 on top of the yeast layer. As negative controls, separate discs were loaded with LB and
671 water. The plate was incubated at 30°C for another 24 h, and then imaged. A zone of
672 inhibition around the discs indicated antifungal activity.

673

674 **Preparation of bacterial membranes**. Cells were grown for 16 h at 30 °C on TBAB
675 plates. The cells were then scraped from the plates and resuspended to OD_{600} = 0.03 in
676 50-mL CAMM supplemented with 50 µg/mL histidine, 50 µg/mL methionine, 50 µg/mL
677 tryptophan, 20 mM sorbitol, and 2% TB. The cells were grown at 37 °C with aeration until
678 they reach mid-exponential phase. The cells were then diluted 1:10 (v/v) into 50 mL
679 CAMM media and grown till mid-exponential phase. The cells were again diluted to an
680 OD_{600} of 0.01 in 50 mL media and grown till mid-exponential phase. Finally, the cultures
681 were diluted 1:10 (v/v) into multiple flasks containing 50 mL media and grown with shaking
682 at 37 °C until an OD_{600} of 0.6. The cells were then harvested by centrifugation at 9900 x
683 *g* for 15 min and washed 3 times with 1 M KCl to remove extracellular proteases. Cells
684 were resuspended in sonication buffer+ (10 mM potassium phosphate (pH 7), 10 mM

685 $MgCl_2$, 1 mM EDTA, 0.3 mM DTT, 20 mM KCl, 1 mM glutamate, 2 mM
686 phenylmethanesulphonyl fluoride, and 20% glycerol). EDTA and
687 phenylmethanesulphonyl fluoride were added as protease inhibitors. Cells were
688 sonicated, and the cell debris was removed by centrifugation at 17,600 x *g* at 4 °C for 15
689 min. Bacterial membranes were removed by centrifugation at 120,000 x *g* for 2 h at 4 °C
690 in a Beckman 70 Ti rotor. Pelleted membranes were resuspended in MT buffer (10 mM
691 potassium phosphate (pH 7), 1 mM $MgCl_2$, 0.1 mM EDTA, and 1 mM 2-mercaptoethanol),
692 and homogenized using a glass/Teflon homogenizer followed by another centrifugation
693 at 120,000 x *g* for 2 h at 4 °C. This step was repeated once more. Finally, the membranes
694 were homogenized in MT buffer at a concentration of 32 mg/mL and stored in small
695 aliquots at -80 °C.
696
697 ***In vitro* assay for receptor-coupled kinase activity.** Reactions consisted of purified
698 *B. subtilis* membranes expressing McpB or HemAT as the sole chemoreceptor and
699 purified CheW, CheA, and CheD prepared in buffer (50 mM Tris, 50 mM KCl, 5 mM $MgCl_2$,
700 pH 7.5) at the following concentrations: 6 μM chemoreceptor, 2 μM CheW, 2 μM CheA
701 kinase, and 2 μM CheD. Ethanol was then added to the mixture at different final
702 concentrations in 20 μL reaction volume. As a negative control, only buffer was added.
703 Reactions were then pre-incubated at 23 °C for 1 h to permit the formation of the
704 chemoreceptor-kinase complex. CheA autophosphorylation was initiated by the addition
705 of [γ-^{32}P] ATP (4000-8000 cpm/pmol) to a final concentration of 0.1 mM. 5 μL aliquots
706 were quenched at 15 s by mixing the reactions with 15 μL of 2X Laemmli sample buffer
707 containing 25 mM EDTA at room temperature, essentially fixing the level of phosphor-

CheA. Initial phosphor-CheA formation rates were analyzed using 12% SDS-PAGE. Gels were dried immediately after electrophoresis and phosphor-CheA was quantified by phosphor-imaging (Molecular Dynamics) and ImageJ (70).

Circular dichroism (CD) spectroscopy. Far UV CD-spectra was measured on a JASCO J-720 spectropolarimeter (Japan Spectroscopic Co., Inc., Tokyo, Japan) with a cuvette of path length 0.1 cm. Prior to measurements, protein samples were dialyzed into 10 mM sodium phosphate buffer (pH 8) and diluted to 2.5 μM. Spectral measurements were carried out in triplicate using a scanning rate of 50 nm/min, 0.1 nm step size with 5 accumulations per sample. A buffer only control sample was used for baseline correction and curves were smoothed according to Savitzky-Golay algorithm (71). Structural analysis was done using BeStSel (72).

Ultraviolet-visible (UV) spectral measurements. All UV-spectral measurements were performed on a Shimadzu UV-1800 spectrophotometer. The UV-spectra of the oxygenated sensing domain of HemAT ($HemAT_N$) protein was measured in aerobic conditions. To measure the UV-spectra of $HemAT_N$ in presence of ethanol, protein samples were first deoxygenated by adding a few grains of sodium dithionite in a glove box. Sodium dithionite-reduced protein samples were then titrated with different doses of ethanol in sealed quartz cuvettes, and the UV-spectra (200 nm to 600 nm) of these samples were immediately recorded in the spectrophotometer.

Saturation-transfer difference nuclear magnetic resonance spectroscopy (STD-NMR). All NMR spectroscopy measurements were performed on a Varian VNMRS instrument at 750 MHz with 5 mm Varian HCN probe at 298 K without sample spinning. Prior to measurements, protein samples were buffer exchanged into PBS (50 mM KH_2PO_4, 20 mM NaCl, pH 7.4) in D_2O using Micro Bio-Spin® Columns with Bio-Gel® P-6 (Bio-Rad Laboratories, Hercules, CA, USA). To avoid aggregation, $HemAT_N$ protein was buffer exchanged into modified PBS (50 mM KH_2PO_4, 300 mM NaCl, pH 8.0) containing 10% D_2O. 50 µM Protein samples were then mixed with the alcohol (final concentration of 3 mM) in a 500 µL solution. ^1H spectra were obtained from 32 scans with a 90-degree pulse and a 2-s relaxation delay. In STD-NMR experiments, the protein samples were selectively saturated at 2.15 ppm with a train of Gaussian pulses of 50 ms duration with 0.1 ms delay and 5 s relaxation delay for a total saturation time of 3 s and 2048 scans. Off-resonance irradiation was applied at 30 ppm. Trim pulse of 50 ms was used to reduce protein background. In the case of $HemAT_N$, the protein sample was saturated at 7.06 ppm and 256 scans were used to obtain spectra. All STD spectra were obtained by internal subtraction via phase cycling after a block size of 8 to reduce artifacts resulted from temperature variation and magnet instability. Control experiments were performed on samples containing only the alcohol without protein. All areas were calculated using MNova V14.1 (by Mestrelab chemistry solutions) in stacked mode.

Structural analysis. Domains of the McpB, McpA, TlpA, and TlpB chemoreceptors from *B. subtilis* were predicted using phmmer search engine on the HMMER web server using the UniProt reference proteomes database with default sequence E value

753 thresholds (73). The amino acid sequences of the cytoplasmic signaling domains were
754 then manually obtained based on the previous large-scale alignment results (10). To
755 identify the three structural subdomains of the cytoplasmic signaling domain, the
756 sequences were then aligned with the amino acid sequences of the corresponding
757 domains from the Tar, Tsr, Trg, and Tap chemoreceptors of *E. coli* using MUSCLE (74)
758 with the default parameter values. Pairwise amino-acid sequence alignments between
759 the protein-pairs (McpA-McpB; McpA-HemAT; and HemAT-YfmS) for chimeric receptor
760 analysis were performed using EMBOSS Water (75). A homology model of the
761 cytoplasmic signaling domain of the McpB dimer (residues 352 to 662) was constructed
762 in Modeller (v-9.23) (76) using the *Thermatoga maritima* Tm113 chemoreceptor (PDB
763 2CH7) as the template (77). Side chain conformations were refined using SCWRL4 (78)
764 and the entire structural model was subsequently refined using the YASARA energy
765 minimization server (79). The resulting Ramachandran plots were verified using Procheck
766 (80). The crystal structure of HemAT sensing domain from *B. subtilis* (PDB 1OR6) (34)
767 was used for visualization. Visualization of all structures was accomplished using the
768 VMD software package (v-1.9.3) (81).
769
770 **Receptor-ligand *in silico* docking experiment.** The putative binding sites for
771 ethanol were determined using Autodock (v-4.0) (82). Briefly, hydrogen atoms were first
772 added to the McpB cytoplasmic signaling domain dimer model, and the number of
773 torsional degrees of freedom for ethanol were set at 1. Autogrid was then used to adjust
774 the position of grid boxes (60 x 60 x 60 points with 0.375 Å spacing for each box) on the

775 ethanol-sensing region (residues 390 to 435). Finally, the Lamarckian genetic algorithm
776 was employed to obtain the best docking site configurations.
777
778 **Molecular dynamics simulations.** All-atom molecular dynamics simulations were
779 conducted using NAMD 2.13 (83) and the CHARMM36 force field (84). Simulations were
780 carried out in the NPT ensemble (pressure = 1 atm, temperature = 310 K) with values for
781 general simulation parameters as previously described (85). The McpB cytoplasmic dimer
782 model was solvated with TIP3P water and 150 mM NaCl using VMD (81), and 165 ethanol
783 molecules (0.316 M) were randomly placed within the simulation box using the *gmx insert-*
784 *molecules* tool. A copy of the system that included the A431S mutation was created, and
785 both the wild-type and mutant McpB/ethanol systems were subjected to a conjugant-
786 gradient energy minimization (2,000 steps) followed by a 10 ns equilibration simulation
787 with protein backbone restraints and 3 x 600 ns unrestrained production simulations.
788
789 **Molecular dynamics simulation analysis.** Density maps representing the average
790 ethanol occupancy were computed using the VolMap plugin in VMD with default settings
791 and averaging over each production simulation for the wild-type and A431S McpB/ethanol
792 systems. To highlight unique binding sites between the two maps, a difference map was
793 computed by subtracting the A431S map from the wild-type using VMD's volutil plugin
794 and removing smaller volumes resulting from slight irregularities in overlapping sites using
795 the 'hide dust' feature in UCSF Chimera. All densities are visualized at an isovalue of 0.03
796 besides the difference map, which used an isovalue of 0.015. Protein-ethanol
797 coordination was computed by measuring the minimum distance between non-hydrogen

798 atoms in each residue and the nearest ethanol molecule; if this distance was less than 4
799 Å, the pair was considered to be in contact. Average coordination values were computed
800 for each residue in the wild-type and A431S mutant McpB/ethanol systems by averaging
801 over all three production simulations at 200 picosecond intervals. Percent changes were
802 obtained by subtracting the values obtained in the latter from the former. Knobs-in-holes
803 packing within the McpB cytoplasmic signaling domain was analyzed using the program
804 SOCKET (86) with a packing cutoff of 7.8 Å (87). For each production simulation, knobs-
805 in-holes packing was assessed at 2-ns intervals over the course of the trajectory, not
806 including the first 100 ns to allow for packing changes resulting from equilibration or the
807 A431S mutation. The occupancy of a particular knob-in-hole interaction over a given
808 simulation was taken as the number of intervals in which it was identified by SOCKET
809 divided by the total number of intervals analyzed in the simulation. The reported knobs-
810 in-holes occupancies were averaged over both McpB monomers and all three production
811 simulations for each McpB/ethanol system; error bars denote one standard deviation from
812 the mean.
813
814 **Simulation of ethanol diffusion in the capillary assay.** Spatiotemporal evolution of
815 ethanol (C) in the capillary assay was modeled using Fick's second law equation with
816 Neumann (no-flux) boundary conditions shown in the equation below:
817 $$\frac{dC}{dt} = D\nabla C$$
818 Initial ethanol concentration (C_0) was set to 50 mM in the capillary and to zero in the pond.
819 Ethanol diffusion coefficient (D) was assumed to be 1.23 x 10^{-3} mm^2/s (88). The above
820 partial differential equation was solved using the finite element method with the help of

821 the FEniCS (v-2019.1.0), an open-source computing platform (89). Briefly, the
822 computation domain consists of capillary and proximal region near the mouth of capillary
823 in the pond. The capillary was modeled as a 10-mm long cylinder with a diameter of 0.2
824 mm attached to an 8-mm long cylinder with diameter of 4 mm, respectively. Gmsh (v-
825 4.5.2) (90) was used to generate the three-dimensional finite element mesh and the XML
826 file of the resulting mesh was produced using the meshio-convert tool available from
827 FEniCS. The implicit Euler method was employed for time integration with step size of Δt
828 = 1 s. A custom Python script was generated for solving the finite-element problem.
829
830 **Data availability**
831 Raw data for all experiments are provided as Data set S1. The Python script for diffusion
832 simulation is provided at https://github.com/paymantohidifar/alcoholtaxis.
833

Acknowledgment

We thank Prof. Jodi A. Hadden-Perilla for discussions surrounding the use of SOCKET. We would also like to thank Dr. Lingyang Zhu, Dr. Dean Olson, and the SCS NMR laboratory at the University of Illinois at Urbana-Champaign for valuable inputs and help with NMR measurements; Dr. Ahmed Hetta and Dr. Issac Caan for help with CD spectroscopy experiments. This work was partially funded by National Institutes of Health Grant GM054365 and by the University of Illinois through the Robert W. Schaefer Faculty Scholar fund.

References

1. Adler J. 1966. Chemotaxis in bacteria. Science 153:708-16.
2. Ortega A, Zhulin IB, Krell T. 2017. Sensory Repertoire of Bacterial Chemoreceptors. Microbiol Mol Biol Rev 81.
3. Rao CV, Ordal GW. 2009. The molecular basis of excitation and adaptation during chemotactic sensory transduction in bacteria. Contrib Microbiol 16:33-64.
4. Rao CV, Glekas GD, Ordal GW. 2008. The three adaptation systems of Bacillus subtilis chemotaxis. Trends Microbiol 16:480-7.
5. Kristich CJ, Glekas GD, Ordal GW. 2003. The conserved cytoplasmic module of the transmembrane chemoreceptor McpC mediates carbohydrate chemotaxis in Bacillus subtilis. Mol Microbiol 47:1353-66.
6. Neumann S, Grosse K, Sourjik V. 2012. Chemotactic signaling via carbohydrate phosphotransferase systems in Escherichia coli. Proc Natl Acad Sci U S A 109:12159-64.
7. Umemura T, Matsumoto Y, Ohnishi K, Homma M, Kawagishi I. 2002. Sensing of cytoplasmic pH by bacterial chemoreceptors involves the linker region that connects the membrane-spanning and the signal-modulating helices. J Biol Chem 277:1593-8.
8. Bi S, Jin F, Sourjik V. 2018. Inverted signaling by bacterial chemotaxis receptors. Nat Commun 9:2927.
9. Vaknin A, Berg HC. 2006. Osmotic stress mechanically perturbs chemoreceptors in Escherichia coli. Proc Natl Acad Sci U S A 103:592-6.

10. Alexander RP, Zhulin IB. 2007. Evolutionary genomics reveals conserved structural determinants of signaling and adaptation in microbial chemoreceptors. Proc Natl Acad Sci U S A 104:2885-90.
11. Stewart GG, Panchal CJ, Russell I, Sills AM. 2008. Biology of Ethanol-Producing Microorganisms. Critical Reviews in Biotechnology 1:161-188.
12. Glekas GD, Foster RM, Cates JR, Estrella JA, Wawrzyniak MJ, Rao CV, Ordal GW. 2010. A PAS domain binds asparagine in the chemotaxis receptor McpB in Bacillus subtilis. J Biol Chem 285:1870-8.
13. Glekas GD, Mulhern BJ, Kroc A, Duelfer KA, Lei V, Rao CV, Ordal GW. 2012. The Bacillus subtilis chemoreceptor McpC senses multiple ligands using two discrete mechanisms. J Biol Chem 287:39412-8.
14. Ordal GW, Villani DP, Gibson KJ. 1977. Amino acid chemoreceptors of Bacillus subtilis. J Bacteriol 129:156-65.
15. Bohin JP, Rigomier D, Schaeffer P. 1976. Ethanol sensitivity of sporulation in Bacillus subtilis: a new tool for the analysis of the sporulation process. J Bacteriol 127:934-40.
16. Walukiewicz HE, Tohidifar P, Ordal GW, Rao CV. 2014. Interactions among the three adaptation systems of Bacillus subtilis chemotaxis as revealed by an in vitro receptor-kinase assay. Mol Microbiol 93:1104-18.
17. Cannistraro VJ, Glekas GD, Rao CV, Ordal GW. 2011. Cellular stoichiometry of the chemotaxis proteins in Bacillus subtilis. J Bacteriol 193:3220-7.
18. Reid MF, Fewson CA. 1994. Molecular characterization of microbial alcohol dehydrogenases. Crit Rev Microbiol 20:13-56.

19. Zhang X, Hughes JG, Subuyuj GA, Ditty JL, Parales RE. 2019. Chemotaxis of Pseudomonas putida F1 to Alcohols Is Mediated by the Carboxylic Acid Receptor McfP. Appl Environ Microbiol 85.
20. Alexandre G. 2010. Coupling metabolism and chemotaxis-dependent behaviours by energy taxis receptors. Microbiology 156:2283-2293.
21. Nakano MM, Dailly YP, Zuber P, Clark DP. 1997. Characterization of anaerobic fermentative growth of Bacillus subtilis: identification of fermentation end products and genes required for growth. J Bacteriol 179:6749-55.
22. Nakano MM, Hulett FM. 1997. Adaptation of Bacillus subtilis to oxygen limitation. FEMS Microbiol Lett 157:1-7.
23. Leonardo MR, Cunningham PR, Clark DP. 1993. Anaerobic regulation of the adhE gene, encoding the fermentative alcohol dehydrogenase of Escherichia coli. J Bacteriol 175:870-8.
24. Walukiewicz HE, Ordal GW, Rao CV. 2018. In Vitro Assay for Measuring Receptor-Kinase Activity in the Bacillus subtilis Chemotaxis Pathway. Methods Mol Biol 1729:95-105.
25. Tohidifar P, Plutz MJ, Ordal GW, Rao CV. 2020. The Mechanism of Bidirectional pH Taxis in Bacillus subtilis. J Bacteriol 202.
26. Bi S, Pollard AM, Yang Y, Jin F, Sourjik V. 2016. Engineering Hybrid Chemotaxis Receptors in Bacteria. ACS Synth Biol 5:989-1001.
27. Weerasuriya S, Schneider BM, Manson MD. 1998. Chimeric chemoreceptors in Escherichia coli: signaling properties of Tar-Tap and Tap-Tar hybrids. J Bacteriol 180:914-20.

911 28. Hou S, Larsen RW, Boudko D, Riley CW, Karatan E, Zimmer M, Ordal GW, Alam
912 M. 2000. Myoglobin-like aerotaxis transducers in Archaea and Bacteria. Nature
913 403:540-4.
914 29. Rahman H, King RM, Shewell LK, Semchenko EA, Hartley-Tassell LE, Wilson JC,
915 Day CJ, Korolik V. 2014. Characterisation of a multi-ligand binding chemoreceptor
916 CcmL (Tlp3) of Campylobacter jejuni. PLoS Pathog 10:e1003822.
917 30. Mayer M, Meyer B. 1999. Characterization of Ligand Binding by Saturation
918 Transfer Difference NMR Spectroscopy. Angew Chem Int Ed Engl 38:1784-1788.
919 31. Mayer M, Meyer B. 2001. Group epitope mapping by saturation transfer difference
920 NMR to identify segments of a ligand in direct contact with a protein receptor. J
921 Am Chem Soc 123:6108-17.
922 32. Cala O, Krimm I. 2015. Ligand-Orientation Based Fragment Selection in STD NMR
923 Screening. J Med Chem 58:8739-42.
924 33. Viegas A, Manso Jo, Nobrega FL, Cabrita EJ. 2011. Saturation-Transfer
925 Difference (STD) NMR: A Simple and Fast Method for Ligand Screening and
926 Characterization of Protein Binding. Journal of Chemical Education 88:990-994.
927 34. Zhang W, Phillips GN, Jr. 2003. Structure of the oxygen sensor in Bacillus subtilis:
928 signal transduction of chemotaxis by control of symmetry. Structure 11:1097-110.
929 35. Zhang W, Olson JS, Phillips GN, Jr. 2005. Biophysical and kinetic characterization
930 of HemAT, an aerotaxis receptor from Bacillus subtilis. Biophys J 88:2801-14.
931 36. Hou S, Freitas T, Larsen RW, Piatibratov M, Sivozhelezov V, Yamamoto A,
932 Meleshkevitch EA, Zimmer M, Ordal GW, Alam M. 2001. Globin-coupled sensors:

933 a class of heme-containing sensors in Archaea and Bacteria. Proc Natl Acad Sci
934 U S A 98:9353-8.
935 37. Aono S, Kato T, Matsuki M, Nakajima H, Ohta T, Uchida T, Kitagawa T. 2002.
936 Resonance Raman and ligand binding studies of the oxygen-sensing signal
937 transducer protein HemAT from Bacillus subtilis. J Biol Chem 277:13528-38.
938 38. Mohd Azhar SH, Abdulla R, Jambo SA, Marbawi H, Gansau JA, Mohd Faik AA,
939 Rodrigues KF. 2017. Yeasts in sustainable bioethanol production: A review.
940 Biochem Biophys Rep 10:52-61.
941 39. Russo F, Cabrita M, Feio SS, Moiteiro C, Tavares R, Marcelo-Curto MJ, Roseiro
942 JC. 2002. Antifungal Activity of Bacillus Species and Pseudomonas aeruginosa
943 Against Filamentous Fungi and Yeasts, p 249-253, Natural Products in the New
944 Millennium: Prospects and Industrial Application doi:10.1007/978-94-015-9876-
945 7_26.
946 40. Leifert C, Li H, Chidburee S, Hampson S, Workman S, Sigee D, Epton HA, Harbour
947 A. 1995. Antibiotic production and biocontrol activity by Bacillus subtilis CL27 and
948 Bacillus pumilus CL45. J Appl Bacteriol 78:97-108.
949 41. Podile AR, Prakash AP. 1996. Lysis and biological control of Aspergillus niger by
950 Bacillus subtilis AF 1. Can J Microbiol 42:533-8.
951 42. Ohimain EI. 2016. Methanol contamination in traditionally fermented alcoholic
952 beverages: the microbial dimension. Springerplus 5:1607.
953 43. Yasueda H, Kawahara Y, Sugimoto S. 1999. Bacillus subtilis yckG and yckF
954 encode two key enzymes of the ribulose monophosphate pathway used by
955 methylotrophs, and yckH is required for their expression. J Bacteriol 181:7154-60.

956 44. Allard-Massicotte R, Tessier L, Lecuyer F, Lakshmanan V, Lucier JF, Garneau D,
957 Caudwell L, Vlamakis H, Bais HP, Beauregard PB. 2016. Bacillus subtilis Early
958 Colonization of Arabidopsis thaliana Roots Involves Multiple Chemotaxis
959 Receptors. mBio 7.
960 45. Yang Y, A MP, Hofler C, Poschet G, Wirtz M, Hell R, Sourjik V. 2015. Relation
961 between chemotaxis and consumption of amino acids in bacteria. Mol Microbiol
962 96:1272-82.
963 46. Tso WW, Adler J. 1974. Negative chemotaxis in Escherichia coli. J Bacteriol
964 118:560-76.
965 47. Oku S, Hida A, Mattana T, Tajima T, Nakashimada Y, Kato J. 2017. Involvement
966 of many chemotaxis sensors in negative chemotaxis to ethanol in Ralstonia
967 pseudosolanacearum Ps29. Microbiology 163:1880-1889.
968 48. Harris RA, Trudell JR, Mihic SJ. 2008. Ethanol's molecular targets. Sci Signal
969 1:re7.
970 49. Dudley R. 2004. Ethanol, Fruit Ripening, and the Historical Origins of Human
971 Alcoholism in Primate Frugivory. Integrative and Comparative Biology 44:315-323.
972 50. Alpi A, Beevers H. 1983. Effects of O2 Concentration on Rice Seedlings. Plant
973 Physiology 71:30-34.
974 51. Setter T. 1994. Relationship between Coleoptile Elongation and Alcoholic
975 Fermentation in Rice Exposed to Anoxia. II. Cultivar Differences. Annals of Botany
976 74:273-279.
977 52. Kato-Noguchi H, Kugimiya T. 2001. Effects of ethanol on growth of rice seedlings.
978 Plant Growth Regulation 35:93-96.

53. Mihic SJ, Ye Q, Wick MJ, Koltchine VV, Krasowski MD, Finn SE, Mascia MP, Valenzuela CF, Hanson KK, Greenblatt EP, Harris RA, Harrison NL. 1997. Sites of alcohol and volatile anaesthetic action on GABA(A) and glycine receptors. Nature 389:385-9.

54. Taly A, Delarue M, Grutter T, Nilges M, Le Novere N, Corringer PJ, Changeux JP. 2005. Normal mode analysis suggests a quaternary twist model for the nicotinic receptor gating mechanism. Biophys J 88:3954-65.

55. Cheng MH, Cascio M, Coalson RD. 2007. Homology modeling and molecular dynamics simulations of the alpha1 glycine receptor reveals different states of the channel. Proteins 68:581-93.

56. Ren H, Zhao Y, Wu M, Dwyer DS, Peoples RW. 2017. Two adjacent phenylalanines in the NMDA receptor GluN2A subunit M3 domain interactively regulate alcohol sensitivity and ion channel gating. Neuropharmacology 114:20-33.

57. Shahidullah M, Harris T, Germann MW, Covarrubias M. 2003. Molecular features of an alcohol binding site in a neuronal potassium channel. Biochemistry 42:11243-52.

58. Kruse SW, Zhao R, Smith DP, Jones DN. 2003. Structure of a specific alcohol-binding site defined by the odorant binding protein LUSH from Drosophila melanogaster. Nat Struct Biol 10:694-700.

59. Howard RJ, Murail S, Ondricek KE, Corringer PJ, Lindahl E, Trudell JR, Harris RA. 2011. Structural basis for alcohol modulation of a pentameric ligand-gated ion channel. Proc Natl Acad Sci U S A 108:12149-54.

60. Dwyer* DS, Bradley RJ. 2000. Chemical properties of alcohols and their protein binding sites. Cellular and Molecular Life Sciences 57:265-275.
61. Khrustalev VV, Khrustaleva TA, Lelevich SV. 2017. Ethanol binding sites on proteins. Journal of Molecular Graphics and Modelling 78:187-194.
62. Altenbuchner J. 2016. Editing of the Bacillus subtilis Genome by the CRISPR-Cas9 System. Appl Environ Microbiol 82:5421-7.
63. Labun K, Montague TG, Krause M, Torres Cleuren YN, Tjeldnes H, Valen E. 2019. CHOPCHOP v3: expanding the CRISPR web toolbox beyond genome editing. Nucleic Acids Res 47:W171-W174.
64. Engler C, Kandzia R, Marillonnet S. 2008. A one pot, one step, precision cloning method with high throughput capability. PLoS One 3:e3647.
65. Gibson DG, Young L, Chuang RY, Venter JC, Hutchison CA, 3rd, Smith HO. 2009. Enzymatic assembly of DNA molecules up to several hundred kilobases. Nat Methods 6:343-5.
66. Anagnostopoulos C, Spizizen J. 1961. Requirements for Transformation in Bacillus Subtilis. J Bacteriol 81:741-6.
67. Ordal GW, Gibson KJ. 1977. Chemotaxis toward amino acids by Bacillus subtilis. J Bacteriol 129:151-5.
68. Kagi JH, Vallee BL. 1960. The role of zinc in alcohol dehydrogenase. V. The effect of metal-binding agents on thestructure of the yeast alcohol dehydrogenase molecule. J Biol Chem 235:3188-92.
69. Balouiri M, Sadiki M, Ibnsouda SK. 2016. Methods for in vitro evaluating antimicrobial activity: A review. J Pharm Anal 6:71-79.

70. Schneider CA, Rasband WS, Eliceiri KW. 2012. NIH Image to ImageJ: 25 years of image analysis. Nat Methods 9:671-5.
71. Savitzky A, Golay MJE. 1964. Smoothing and Differentiation of Data by Simplified Least Squares Procedures. Analytical Chemistry 36:1627-1639.
72. Micsonai A, Wien F, Bulyaki E, Kun J, Moussong E, Lee YH, Goto Y, Refregiers M, Kardos J. 2018. BeStSel: a web server for accurate protein secondary structure prediction and fold recognition from the circular dichroism spectra. Nucleic Acids Res 46:W315-W322.
73. Potter SC, Luciani A, Eddy SR, Park Y, Lopez R, Finn RD. 2018. HMMER web server: 2018 update. Nucleic Acids Res 46:W200-W204.
74. Edgar RC. 2004. MUSCLE: a multiple sequence alignment method with reduced time and space complexity. BMC Bioinformatics 5:113.
75. Rice P, Longden I, Bleasby A. 2000. EMBOSS: the European Molecular Biology Open Software Suite. Trends Genet 16:276-7.
76. Webb B, Sali A. 2016. Comparative Protein Structure Modeling Using MODELLER. Curr Protoc Bioinformatics 54:5 6 1-5 6 37.
77. Park SY, Borbat PP, Gonzalez-Bonet G, Bhatnagar J, Pollard AM, Freed JH, Bilwes AM, Crane BR. 2006. Reconstruction of the chemotaxis receptor-kinase assembly. Nat Struct Mol Biol 13:400-7.
78. Krivov GG, Shapovalov MV, Dunbrack RL, Jr. 2009. Improved prediction of protein side-chain conformations with SCWRL4. Proteins 77:778-95.
79. Krieger E, Joo K, Lee J, Lee J, Raman S, Thompson J, Tyka M, Baker D, Karplus K. 2009. Improving physical realism, stereochemistry, and side-chain accuracy in

homology modeling: Four approaches that performed well in CASP8. Proteins 77 Suppl 9:114-22.

80. Laskowski RA, MacArthur MW, Moss DS, Thornton JM. 1993. PROCHECK: a program to check the stereochemical quality of protein structures. Journal of Applied Crystallography 26:283-291.

81. Humphrey W, Dalke A, Schulten K. 1996. VMD: Visual molecular dynamics. Journal of Molecular Graphics 14:33-38.

82. Morris GM, Huey R, Lindstrom W, Sanner MF, Belew RK, Goodsell DS, Olson AJ. 2009. AutoDock4 and AutoDockTools4: Automated docking with selective receptor flexibility. J Comput Chem 30:2785-91.

83. Phillips JC, Braun R, Wang W, Gumbart J, Tajkhorshid E, Villa E, Chipot C, Skeel RD, Kale L, Schulten K. 2005. Scalable molecular dynamics with NAMD. J Comput Chem 26:1781-802.

84. Huang J, MacKerell AD, Jr. 2013. CHARMM36 all-atom additive protein force field: validation based on comparison to NMR data. J Comput Chem 34:2135-45.

85. Cassidy CK, Himes BA, Sun D, Ma J, Zhao G, Parkinson JS, Stansfeld PJ, Luthey-Schulten Z, Zhang P. 2020. Structure and dynamics of the E. coli chemotaxis core signaling complex by cryo-electron tomography and molecular simulations. Commun Biol 3:24.

86. Walshaw J, Woolfson DN. 2001. Socket: a program for identifying and analysing coiled-coil motifs within protein structures. J Mol Biol 307:1427-50.

87. Swain KE, Gonzalez MA, Falke JJ. 2009. Engineered socket study of signaling through a four-helix bundle: evidence for a yin-yang mechanism in the kinase control module of the aspartate receptor. Biochemistry 48:9266-77.

88. Hills EE, Abraham MH, Hersey A, Bevan CD. 2011. Diffusion coefficients in ethanol and in water at 298K: Linear free energy relationships. Fluid Phase Equilibria 303:45-55.

89. Logg A, Mardal K-A, Wells G (ed). 2012. Automated Solution of Differential Equations by the Finite Element Method.

90. Geuzaine C, Remacle J-F. 2009. Gmsh: A 3-D finite element mesh generator with built-in pre- and post-processing facilities. International Journal for Numerical Methods in Engineering 79:1309-1331.

91. Ullah AH, Ordal GW. 1981. In vivo and in vitro chemotactic methylation in Bacillus subtilis. J Bacteriol 145:958-65.

92. Kristich CJ, Ordal GW. 2002. Bacillus subtilis CheD is a chemoreceptor modification enzyme required for chemotaxis. J Biol Chem 277:25356-62.

1085 **TABLE 1.** Strains used in this study.

Strain	Relevant genotype or description	Reference
5-alpha	*E. coli* cloning host	New England Biolabs
BL21(DE3)	*E. coli* protease deficient expression host	Novagen
GBS111	*Saccharomyces cerevisiae CEN.PK113-7D*	
NCBI3610	Undomesticated wild type *B. subtilis* isolate	
OI3269	*Bacillus subtilis 168, trpC2*	
OI1085	*trpF7 hisH2 metC133 che*$^{+}$	(91)
PTS375	*ΔcheC ΔcheV*	This work
PTS097	Δ*cheC*	(25)
PTS135	Δ*cheV*	(25)
PTS185	*ΔmcpB*	(25)
PTS328	*ΔhemAT*	This work
PTS238	Δ*mcpB ΔhemAT*	This work
OI3545	Δ10*mcp, Erm*^{R}*, Cm*^{R}*, Kan*^{R} *,che+*	(28)
OI3921	OI3545 *amyE5720::mcpA, Spc*^{R}	(92)
OI3605	OI3545 *amyE5720::mcpB, Spc*^{R}	(5)
OI3974	OI3545 *amyE5720::mcpC, Spc*^{R}	(5)
OI4474	OI3545 *amyE5720::tlpA, Spc*^{R}	(25)
OI4475	OI3545 *amyE5720::tlpB, Spc*^{R}	(25)
OI4483	OI3545 *amyE5720::tlpC, Spc*^{R}	(25)
OI4476	OI3545 *amyE5720::yfmS, Spc*^{R}	(25)
OI4477	OI3545 *amyE5720::yvaQ, Spc*^{R}	(25)
OI4482	OI3545 *amyE5720::hemAT, Spc*^{R}	(25)
OI4479	OI3545 *amyE5720::yoaH, Spc*^{R}	(25)
PTS522	OI3545 *amyE5720::mcpB[M1-V287] mcpA[L287-E661]*	This work
PTS529	OI3545 *amyE5720::mcpB[M1-Q359] mcpA[D359-E661]*	This work
GBS103	OI3545 *amyE5720::mcpB[M1-A374] mcpA[S374-E661]*	This work
GBS104	OI3545 *amyE5720::mcpB[M1-N397] mcpA[E397-E661]*	This work
GBS142	OI3545 *amyE5720:: mcpB[M1-Q423] mcpA[A423-E661]*	This work
GBS090	OI3545 *amyE5720::mcpB[M1-I433] mcpA[Q433-E661]*	This work
GBS091	OI3545 *amyE5720::mcpB[M1-I481] mcpA[Q433-E661]*	This work
PTS252	OI3545 *amyE5720::mcpA[M1-Q358] mcpB[D359-E662]*	This work
GBS149	OI3545 *amyE5720:: mcpB[A431S]*	This work
GBS176	OI3545 *amyE5720:: mcpB[T424A]*	This work
GBS175	OI3545 *amyE5720:: mcpB[D427T]*	This work
GBS158	OI3545 *amyE5720:: mcpB[E581Q]*	This work
GBS170	OI3545 *amyE5720:: mcpB[K585E]*	This work
GBS192	OI3545 *amyE5720:: mcpB[399K]*	This work

1086

1087 **TABLE 2.** Plasmids used in this study.

Plasmid	Description	Reference
pET28a (+)	His-tagged cloning vector for protein purification; Kan^R	Novagen
pJSpe	Modified pJOE8999 optimized for Gibson assembly of homology templates; AmpR, Kan^R	(25)
pPT037	pJSpe::*cheV* (for *cheV* knockout)	(25)
pPT058	pJSpe::*mcpB* (for *mcpB* knockout)	(25)
pPT053	pJSpe::*hemAT* (for *hemAT* knockout)	This work
pAIN750	*B. subtilis* empty vector for integration at *amyE*; Amp^R, Spc^R	(92)
pPT200	pAIN750*::mcpB[M1-V287] mcpA[L287-E661]*	This work
pPT205	pAIN750*::mcpB[M1-Q359] mcpA[D359-E661]*	This work
pGB42	pAIN750*::mcpB[M1-A374] mcpA[S374-E661]*	This work
pGB43	pAIN750*::mcpB[M1-N397] mcpA[E397-E661]*	This work
pGB34	pAIN750*::mcpB[M1-I433] mcpA[Q433-E661]*	This work
pGB64	pAIN750*::mcpB[M1-Q423] mcpA[A423-E661]*	This work
pGB35	pAIN750*::mcpB[M1-L481] mcpA[R481-E661]*	This work
pPT086	pAIN750*::mcpA[M1-Q358]-mcpB[D359-E662]*	This work
pGB65	pAIN750*::mcpB[A431S]*	This work
pGB83	pAIN750*::mcpB[T424A]*	This work
pGB82	pAIN750*::mcpB[D427T]*	This work
pGB67	pAIN750*::mcpB[E581Q]*	This work
pGB79	pAIN750*::mcpB[K585E]*	This work
pGB94	pAIN750*::mcpB[E399K]*	This work
pPT262	6xHis-C terminal McpB expression plasmid, pET28(a)::$mcpB_C$	This work
pGB78	6xHis-C terminal $McpB_C$[A431S] expression plasmid, pET28(a)::$mcpB_C$*[A431S]*	This work
pGB53	6xHis-C terminal McpA expression plasmid, pET28(a)::$mcpA_C$	This work
pGEX-6p-2::*cheA*	GST-CheA overexpression plasmid	(16)
pGEX-6p-2::*cheW*	GST-CheW overexpression plasmid	(16)
pGEX-6p-2::*cheD*	GST-CheD overexpression plasmid	(16)
pGB46	6xHis-C terminal HemAT expression plasmid, pET28(a)::$hemAT_S$	This work
pSP03	6xHis-N terminal HemAT expression plasmid, pET28(a)::$hemAT_N$	This work

1088

Figure Legends

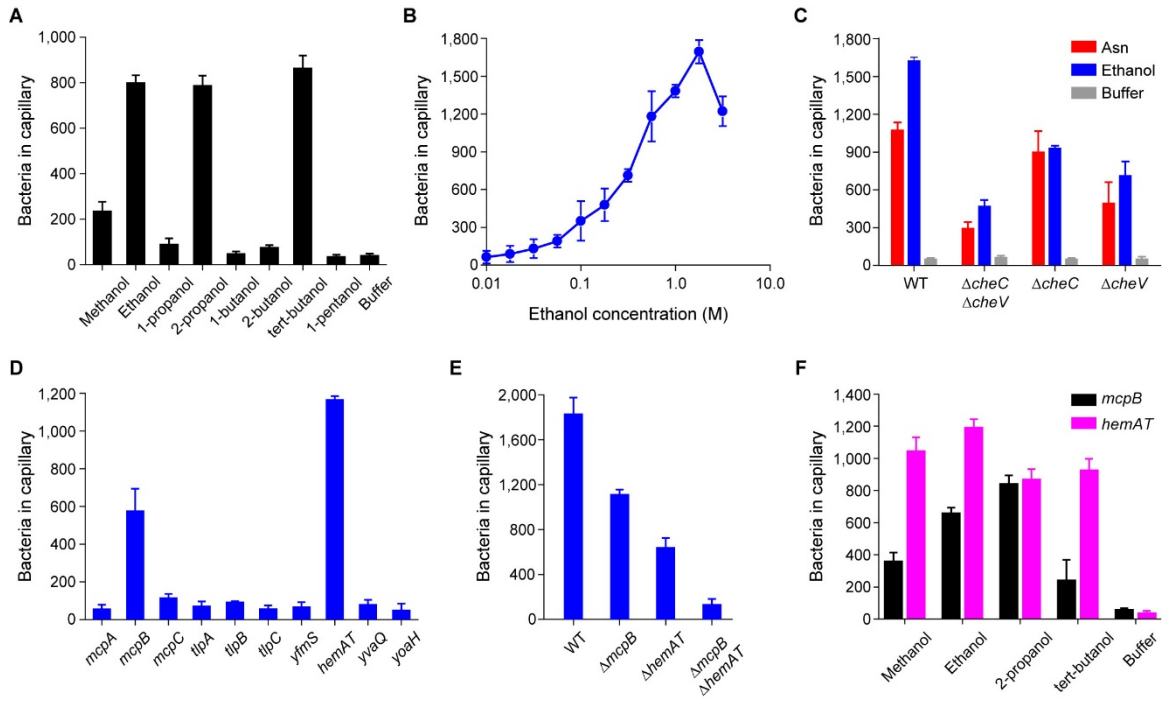

FIG 1. *B. subtilis* exhibits chemotaxis toward short-chain alcohols. (A) Responses of the wild-type strain to 0.5 M short-chain alcohols with increasing chain lengths (C1 to C5). (B) Dose-dependent response of the wild-type strain to increasing concentration of ethanol. (C) Responses of adaptation-deficient mutants to ethanol and asparagine. (D) Responses of mutants expressing single chemoreceptors to ethanol. (E) Responses of mutants lacking key chemoreceptors to ethanol. (F) Responses of mutants expressing McpB or HemAT as their sole chemoreceptor to short-chain alcohols. In these experiments, ethanol and asparagine concentrations were 1.78 M and 3.16 μM, respectively, unless otherwise mentioned. Negative control responses of the strains expressing single chemoreceptor to buffer were all under 100 colonies per capillary. Error bars denote the standard deviations from three biological replicates performed on three separate days.

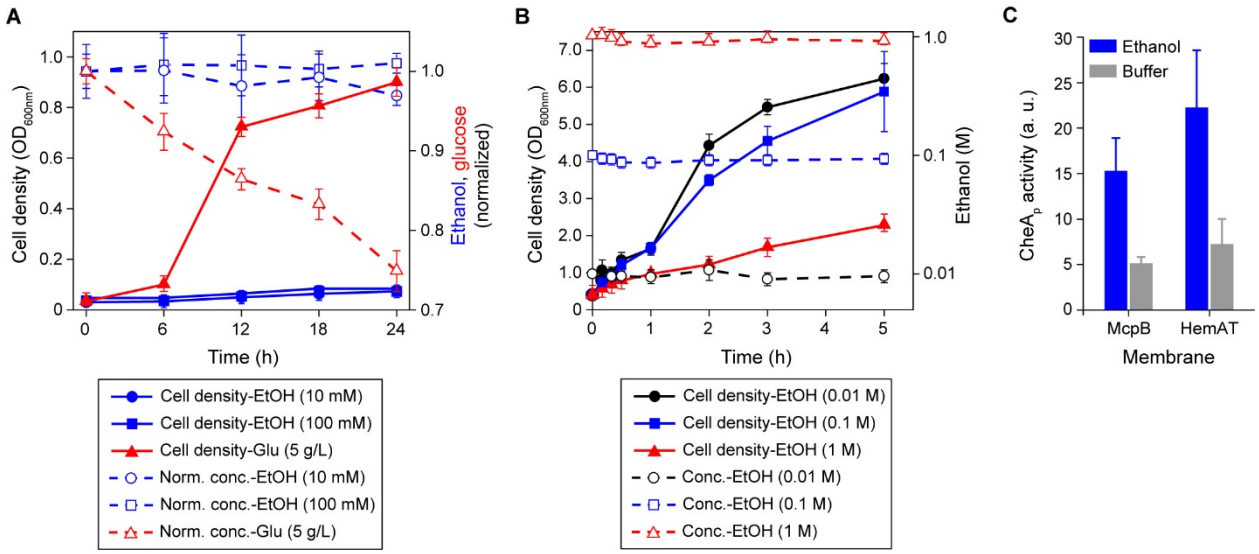

FIG 2. *B. subtilis* chemotaxis to ethanol is independent of its metabolism. (A) Cell growth in minimal medium supplemented with 10 mM ethanol (blue solid circles), 100 mM ethanol (blue solid squares), and 5 g/L glucose (red solid triangles) tested as a positive control. Dashed lines with the corresponding symbols depict normalized concentrations of chemicals measured over the course of 24 h. (B) Cell growth in rich medium containing 10 mM ethanol (black sold circles), 100 mM ethanol (blue solid squares), and 1 M ethanol (red solid triangles). Dashed lines with open symbols depict absolute concentration of ethanol measured at three different conditions over the course of 5 h. (C) Levels of phosphorylated CheA kinase complexed with CheW, CheD, and McpB or HemAT within the isolated membranes, in presence of 1 M ethanol or buffer, as negative control. Error bars denote the standard deviations from three biological replicates performed on three separate days; *P<0.05 (two-sided t-test, correction for unequal variances was applied).

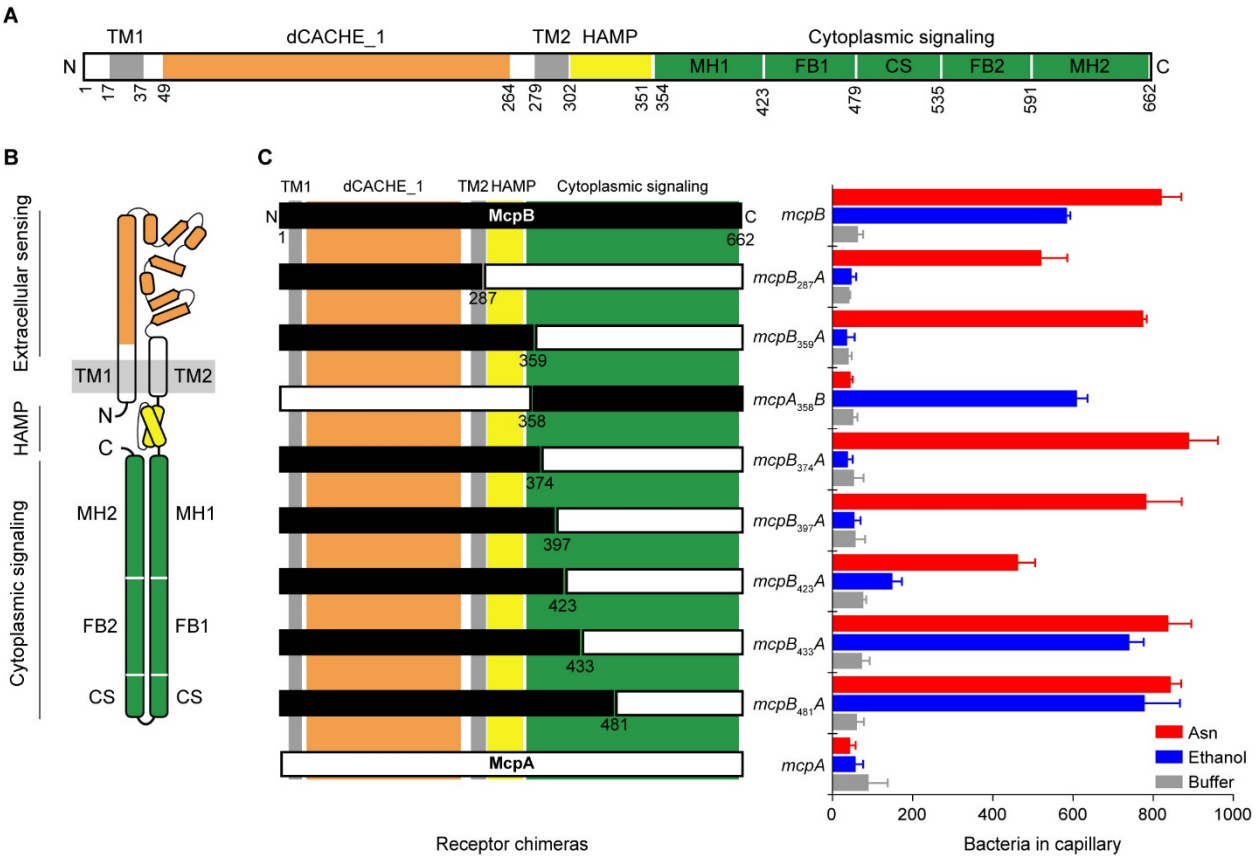

FIG 3. McpB cytoplasmic signaling domain is involved in ethanol sensing. (A) Domain structure of McpB, McpA, TlpA, and TlpB. All four chemoreceptors consist of an extracellular sensing domain with dCACHE_1 structure (orange) followed by transmembrane, TM1 and TM2 (gray), HAMP (yellow), and cytoplasmic signaling (green) domains. Three subdomains of the cytoplasmic signaling domain classified as methylation (adaptation) helices (MH), flexible (coupling) bundle (FB), and conserved signaling (protein contact region) (CS) tip are shown. (B) Cartoon structure of a monomer of the chemoreceptors. (C) Responses of mutants expressing chimeric receptors between McpA (white) and McpB (black) to 1.78 M ethanol, 3.16 μM asparagine, and buffer. Error bars denote the standard deviations from three biological replicates performed on three separate days.

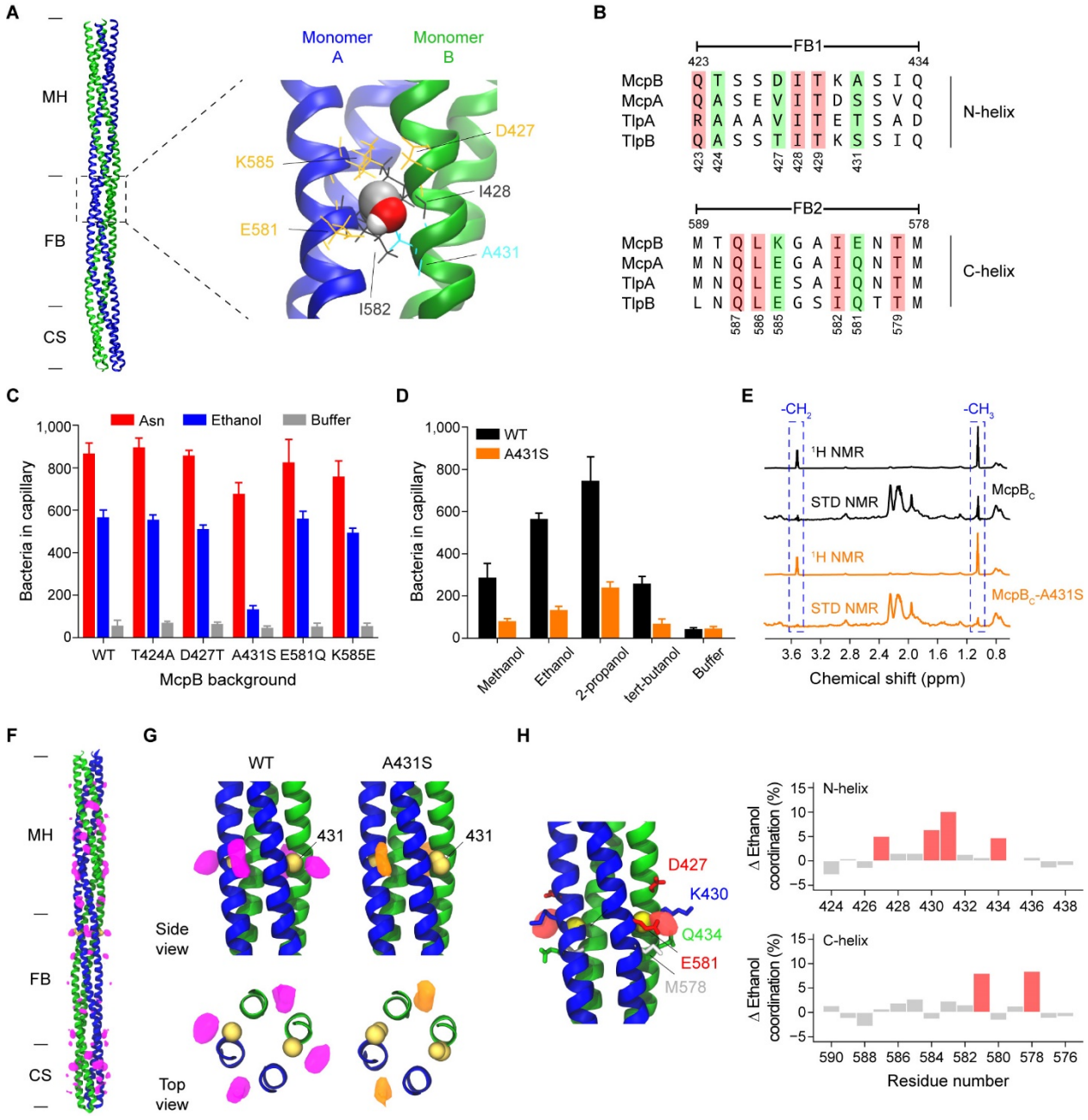

1131

1132 **FIG 4. Alcohols are directly sensed by the cytoplasmic signaling domain of McpB**

1133 (A) A putative binding site within the primary ethanol-sensing region spanning residues

1134 (423 to 433) on the N-helix and the neighboring residues (579 to 589) on the C-helix of

1135 the McpB cytoplasmic signaling domain. (B) Amino acid sequence alignment of the

primary ethanol-sensing region for McpB and the corresponding regions on McpA, TlpA, and TlpB. (C) Responses of strains expressing McpB mutants as their sole chemoreceptors to 1.78 M ethanol, 3.16 μM asparagine, and buffer. (D) Responses of strains expressing wild-type McpB and the McpB-A431S mutant as their sole chemoreceptor to 1.78 M short-chain alcohols and buffer. (E) ^{1}H and STD-NMR spectra for 50 μM wild-type and mutant (A431S) recombinant McpB cytoplasmic region ($McpB_C$) spanning residues (305 to 662). Two peaks at 1.05 ppm and 3.51 ppm (shown inside dashed boxes) respectively correspond to $-CH_3$ and $-CH_2$ epitopes of ethanol. (F) Density map of the average ethanol occupancy (purple) along the wild-type McpB cytoplasmic signaling domain ($McpB_C$) spanning residues 352 to 662, as predicted by MD simulation. (G) Enlarged side and top views of the ethanol occupancy surrounding the residue 431 (yellow) in the wild-type (purple) and the A431S mutant (orange) $McpB_C$. (H) Difference map (red density) between the wild-type and the A431S mutant $McpB_C$ surrounding the residue 431, highlighting the loss of an inter-monomer ethanol binding site in the A431S mutant. Changes in protein-ethanol coordination highlight the putative amino-acid residues (red bars) involved in ethanol binding. Error bars reported in panels C and D denote the standard deviations from three biological replicates performed on three separate days. Ethanol occupancy and coordination values are generated from three independent MD simulations.

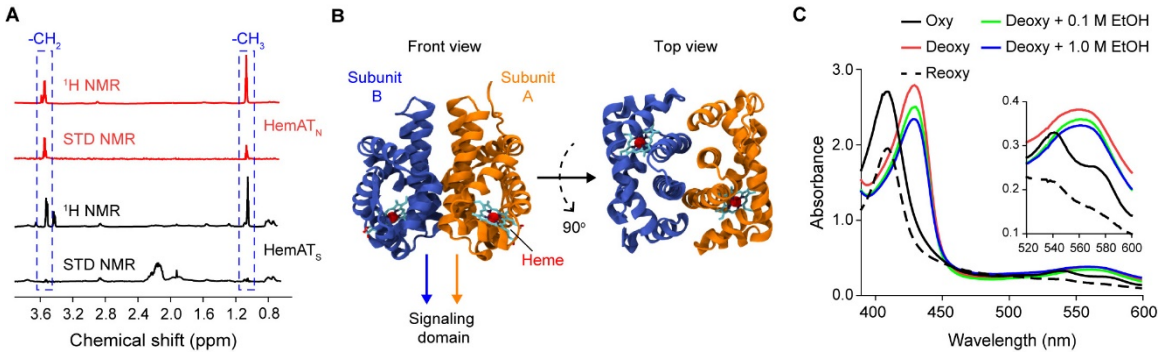

FIG 5. Ethanol directly binds within the helices of the HemAT sensing domain. (A) ^{1}H and STD-NMR spectra for 50 μM recombinant HemAT C-terminal signaling domain ($HemAT_S$) spanning residue (177 to 432) and for 50 μM recombinant HemAT N-terminal sensing domain ($HemAT_N$) spanning residues (1 to 178), in presence of 3 mM ethanol. Two peaks at 1.05 ppm and 3.51 ppm (shown inside dashed boxes) respectively correspond to $-CH_3$ and $-CH_2$ epitopes of ethanol. (B) Crystal structure of the dimeric HemAT sensing domain. (C) UV-spectra of recombinant HemAT N-terminal sensing domain ($HemAT_N$) in absence and presence of molecular oxygen, 0.1 M ethanol, and 1.0 M ethanol.

Supplementary Information

TABLE S1. Putative ethanol-binding sites within the McpB ethanol-sensing region predicted by *in silico* docking experiments.

TABLE S2. Oligonucleotides used in this study

FIG S1. Ethanol induces receptor-coupled kinase activity. Levels of phosphorylated CheA kinase protein complexed with CheW, CheD, and (A) McpB or (B) HemAT chemoreceptors within the isolated membranes, or (C) receptorless membrane (negative control) were measured in presence of increasing ethanol concentrations. 3.16 μM asparagine was used as positive control for membranes containing McpB, and buffer was used as negative control in all experiments.

FIG S2. Amino-acid sequences of three structural subdomains within the cytoplasmic signaling domains of *B. subtilis* transmembrane chemoreceptors. Amino-acid sequences of three structural subdomains, known as methylation helix (MH), flexible bundle (FB), and conserved signaling (CS)), within the cytoplasmic signaling domains of four *B. subtilis* transmembrane chemoreceptors are shown. For comparison, aligned amino-acid sequences of the corresponding subdomains from four *E. coli* transmembrane chemoreceptors are also shown. Characteristic seven-residue repeats (heptads) along the helices are labeled *a* to *g* and the corresponding amino-acid sequences are separated by alternating gray and white colors.

FIG S3. Identification of putative ethanol-binding sites on the cytoplasmic signaling domain of McpB dimer. (A) Five different clusters of putative binding sites within the ethanol sensing region spanning residues (390 to 435) on the N-helix and neighboring residues (577 to 622) on the C-helix of the McpB dimer fragment, predicted by *in silico* docking experiments. Monomers A and B are shown in blue and green, respectively. (B) Amino-acid sequence alignment of the ethanol-sensing region spanning residues (392 to 434) on the N-helix and neighboring residues (578 to 620) on the C-helix of McpB and the corresponding regions on McpA, TlpA, and TlpB. Conserved and non-conserved putative ethanol-binding residues are highlighted in red and green, respectively.

FIG S4. Control experiments for *in-vitro* binding measurements. (A) ^{1}H and STD-NMR spectra for 50 μM recombinant McpA cytoplasmic region ($McpA_C$) spanning residues (304 to 661) with 3 mM ethanol (top red); two peaks at 1.05 ppm and 3.51 ppm (shown inside dashed boxes) respectively correspond to $-CH_3$ and $-CH_2$ epitopes of ethanol. ^{1}H and STD-NMR spectra for 50 μM recombinant McpB cytoplasmic region ($McpB_C$) spanning residues (305 to 662) with 3 mM 1-pentanol (bottom black); peaks shown inside dashed boxes correspond to -CH epitopes of 1-pentanol as indicated by increasing numerical superscripts with 1 corresponding to the first carbon adjacent to hydroxyl group. (B) The CD-spectra of recombinant wild-type and mutant (A431S) $McpB_C$ and recombinant $McpA_C$, reported as mean residual ellipticity (MRE). (C) The CD-spectra of recombinant HemAT signaling domain ($HemAT_S$) spanning residues (177 to 432).

FIG S5. Ethanol and knob-residues occupancy along the McpB coiled-coil. (A) Density maps of the average ethanol occupancy along the wild-type (purple) and the A431S mutant (orange) McpB cytoplasmic signaling domain ($McpB_C$). Differences between the wild-type and the A431S mutant (red density) reveal three distinct putative ethanol binding sites (S1, S2, and S3). Average changes in protein-ethanol coordination highlight the putative amino-acid residues (red bars) involved in ethanol binding in each site. (B) Distribution of knob residues (purple, space-filling) on the McpB cytoplasmic signaling dimer as identified using SOCKET (hole residues are not shown). The close-up depicts the identified knobs nearby the residue Ala^{431} (yellow). In addition to Ala^{431}, residues Ala^{583} and Lys^{585} (cyan) are predicted to have higher average knob occupancies in $McpB_C$-A431S compared to the wild-type $McpB_C$. Data and error bars associated with the knob occupancies in panel b denote the means ± standard deviations from three independent simulations.

FIG S6. Antifungal activity of *B. subtilis* strains. (A) Growth inhibition of *S. cerevisiae* by supernatants from overnight cell cultures of *B. subtilis* OI1085 laboratory chemotaxis strain and undomesticated NCBI 3610 strain is measured using disk diffusion assay. Similar experiments were conducted using only water or LB instead of culture supernatant, as negative controls. (B) Chemotaxis responses of *B. subtilis* OI1085 laboratory chemotaxis strain and undomesticated NCBI 3610 strain to 1.78 M ethanol and buffer. Data and error bars shown in panel b denote the means ± standard deviations from three biological replicates performed on at three separate days.

FIG S7. Simulation of ethanol diffusion in the capillary assay. (A) The three-dimensional finite-element computation domain consists of the ethanol column in the capillary and region near the mouth of capillary in the pond. (B) Normalized ethanol concentration profile along the centerline of the capillary and the pond at three different time points. (C) Normalized ethanol concentration dynamics near mouth of the capillary in the pond during a 30-minute long assay. In panels B and C, ethanol concentration is normalized to initial ethanol concentration in the capillary. Initial ethanol level in the pond was set to zero.

DATA SET S1. Raw data for all experiments and SDS-PAGE images of purified recombinant chemoreceptor proteins reported in the manuscript.